

# Loss of perinuclear theca ACTRT1 causes acrosome detachment and severe male subfertility

Xiao-Zhen Zhang<sup>a, 1</sup>, Lin-Lin Wei<sup>a, 1</sup>, Xiao-Hui Zhang<sup>a</sup>, Hui-Juan Jin<sup>a</sup>,  
Su-Ren Chen<sup>a, \*, ‡</sup>

<sup>a</sup> Education Key Laboratory of Cell Proliferation & Regulation Biology, College of Life Sciences, Beijing Normal University, 100875 Beijing, China

\* Author for correspondence (chensr@bnu.edu.cn)

<sup>1</sup> These authors contributed equally to this work.

<sup>‡</sup> <https://orcid.org/0000-0002-9337-5412>

## ABSTRACT

The perinuclear theca (PT) is a cytoskeletal element encapsulating the sperm nucleus; however, physiological roles of PT in sperm are largely uncertain. Here, we revealed that ACTRT1, ACTRT2, ACTL7A, and ACTL9 proteins interact to form a multimeric complex and localize to the subacrosomal region of spermatids. Furthermore, we engineered *Actrt1*-knockout (KO) mice to define the functions of ACTRT1. Despite the normal sperm count and motility, *Actrt1*-KO males were severely subfertile due to a deficiency in fertilization. Loss of ACTRT1 caused a high incidence of malformed heads and detachment of acrosomes from sperm nuclei, which were caused by the loosened acroplaxome structure during spermiogenesis. Furthermore, *Actrt1*-KO sperm showed reduced ACTL7A and PLC $\zeta$  protein content as a potential cause of fertilization defects. Moreover, we revealed that ACTRT1 anchors developing acrosomes to the nucleus, likely by interacting with the inner acrosomal membrane protein SPACA1 and the nuclear envelope proteins PARP11 and SPATA46. Loss of ACTRT1 weakened the interaction between ACTL7A and SPACA1. Our study and recent findings of *ACTL7A/ACTL9*-deficient sperm together reveal that the sperm PT-specific ARP complex mediates the acrosome-nucleus connection.

**KEY WORDS: Sperm, Perinuclear theca, Actin-related protein, Detached acrosome, Male infertility**

## **INTRODUCTION**

Spermiogenesis refers to the complex processes of the differentiation and maturation of spermatids, including dramatic changes in cell shape. The perinuclear theca (PT) is a special class of cytoskeleton and closely surrounds the nuclei of spermatids/sperm. PT, although structurally continuous, is distinguished in different segments: i) the subacrosomal region (SAR), intercalated between the inner acrosomal membrane (IAM) and the nuclear envelope (NE), ii) PT overlying the equatorial segment (ES), between the plasma membrane and outer acrosomal membrane (OAM), and iii) PT of the postacrosomal sheath (PAS). SAR-PT + ES-PT gives rise to the subacrosomal layer (SAL) of the PT (Okó and Sutovsky, 2009). PT is characterized by resistance to high ionic strength and detergents and by a special (testis-specific) protein composition, including Calicin (Longo et al., 1987), Cylicin I (Hess et al., 1993) and II (Hess et al., 1995), actin-capping proteins CAPZA3 (Geyer et al., 2009) and CP $\beta$ 3 (von Bulow et al., 1997), WW domain-binding proteins WBP2 (Hamilton et al., 2018), and WBP2NL/PAWP (Wu et al., 2007), histone variant H2BL1 (Aul and Okó, 2002), signal transducer and activator of transcription STAT4 (Herrada and Wolgemuth, 1997), phospholipase C PLC $\zeta$  (Hachem et al., 2017), and glutathione S-transferase GSTO2 (Hamilton et al., 2017). SAL-PT and PAS-PT are different in both protein constituents and timing of formation. It has been suggested that SAL proteins originate from acrosomal vesicles during acrosome biogenesis, whereas PAR proteins are translated in the cytoplasmic lobe and then transported via the manchette, concomitantly with spermatid elongation (Okó and Sutovsky, 2009). It has been suggested that SAL-PT is involved in acrosome assembly whereas PAS-PT is involved in sperm-egg interactions at fertilization (Okó and Sutovsky, 2009). However, the physiological roles of PT proteins in sperm are not fully understood.

Actin-related proteins (ARPs) share significant amino acid sequence and basal structure similarities with conventional actins. Several ARPs, such as ACTRT1 (Heid et al., 2002), ACTRT2 (Heid et al., 2002), ACTRT3 (Hara et al., 2008), ACTL7A (Boeda et al., 2011; Xin et al., 2020), ACTL7B (Tanaka et al., 2003), ACTL9 (Dai et al., 2021), and ACTL11 (rodent-specific) (Oh et al., 2013), have been reported to be sperm-specific and selectively localized to the PT structure of sperm heads. ACTL7A interacts with ACTL9 to form a multimeric protein complex (Dai et al., 2021). Despite their expression pattern being well understood, the physiological roles of these ARPs in sperm biology are far from clear. Two recent interesting studies suggest that disruption of *ACTL7A* (Xin et al., 2020) or *ACTL9* (Dai et al., 2021) causes total fertilization failure and male infertility in humans and mice. Transmission electron microscopy analysis further revealed a phenotype of acrosome detachment in *ACTL7A*- and *ACTL9*-mutated sperm (Xin et al., 2020; Dai et al., 2021).

In this study, we generated an *Actrt1*-KO mouse model and found that *Actrt1*-KO males are severely subfertile due to detached acrosomes and a deficiency in fertilization. Intriguingly, the phenotype of *Actrt1*-KO sperm shows a high similarity to *Actl7a*- and *Actl9*-mutated sperm, exhibiting acrosome detachment. Mechanistically, ACTRT1 could form a large complex with ACTRT2, ACTL7A, and ACTL9. ACTRT1 further interacted with the inner acrosomal membrane (IAM) protein SPACA1 and the nuclear envelope (NE) proteins PARP11 and SPATA46. Collectively, these data suggest a critical role of the sperm-specific ARP complex ‘ACTRT1-ACTRT2-ACTL7A-ACTL9’ in anchoring the developing acrosome to the nucleus via the ‘IAM-acroplaxome-NE’ connection.

## RESULTS

### ACTRT1 forms a complex with ACTRT2, ACTL7A, and ACTL9

Western blot analyses of different subcellular components from ACTRT1-Flag-transfected HEK293T cells showed that ACTRT1 was mostly located

in the cytoskeleton, with some cytoplasm and membrane expression (Fig. 1A). This observation is consistent with the concept that ACTRT1 is a protein of sperm cytoskeletal PT (Heid et al., 2002). Likewise, ACTRT2, ACTL7A and ACTL9 were all mainly distributed in the cytoskeletal components (Fig. 1A). To establish the cellular localization of ACTRT1, we performed immunofluorescence staining (Fig. 1B). In round and elongated spermatids, ACTRT1 signals were detected in the subacrosomal region (SAR), and a certain distance existed between ACTRT1 signals and PNA-FITC (an acrosome dye) signals. The ACTRT1 signals in wild-type spermatids were specific because no staining was present using *Actrt1*-KO spermatids (Fig. S1A). Although colocalization of ACTRT1 and ACTL7A was unable to be achieved because both are rabbit antibodies, ACTL7A also exhibited SAR distribution in spermatids (Fig. 1B). Intriguingly, ACTRT1 and ACTL7A were translocated to the postacrosomal sheath (PAS) of mature sperm in the epididymis (Fig. S1B). Although PAS proteins are proposed to be synthesized in the cytoplasmic lobe of elongating spermatids and transported up the manchette for final deposition and assembly in the postacrosomal region (Okamoto and Sutovsky, 2009), some PAS proteins, such as Calicin (Longo et al., 1987; Lecuyer et al., 2000), CAPZA3 (Geyer et al., 2009), ACTRT1 (Heid et al., 2002; this study), and ACTL7A (Boeda et al., 2011; this study), are present in the acroplaxome of spermatids and then translocated to the PAS of spermatozoa. Importantly, Myc-tagged ACTRT1 was immunoprecipitated with Flag-tagged ACTRT2, ACTL7A and ACTL9 in HEK293T cells (Fig. 1C). The interaction between ACTL7A and ACTRT1/2 was further confirmed by endogenous co-IP experiments using mouse testis extracts (Fig. 1D). The assembly of such sperm-specific ARPs into a protein complex suggests that they may play coordinated roles in spermiogenesis.

#### ***Actrt1*-KO male mice are severely subfertile due to a deficiency of fertilization**

To examine the physiological role of ACTRT1 *in vivo*, we generated *Actrt1*-KO mice with the CRISPR/Cas9 system. The *Actrt1* gene has 1 transcript (ENSMUST00000059466.2) and is located on chromosome X. Exon 1 of *Actrt1* is

selected as the knockout region because this region contains all of the coding sequence. *Actrt1*<sup>+/-</sup> females were mated with wild-type males to obtain *Actrt1*<sup>-/-</sup> (*Actrt1*-KO) mice after genotyping PCR. Specific and complete absence of *Actrt1* mRNA in the testis was confirmed by reverse transcription-polymerase chain reaction (RT-PCR) analysis using specific primers for *Actrt1*. The deletion of ACTRT1 protein in *Actrt1*-KO testis was identified by Western blot using anti-ACTRT1 antibody (Fig. 2A). In general, *Actrt1*-KO mice were viable and showed no overt abnormalities. To examine the reproductive ability of *Actrt1*-KO mice, we performed a two-month fertility test using *Actrt1*-KO mice and their littermate wild-type males (*n*=3 each group). Both the pregnancy rate ( $21.57\% \pm 5.06\%$ ) and pups ( $2.33 \pm 0.42$ ) that were born from *Actrt1*-KO males were significantly reduced compared with those from wild-type males (pregnancy rate:  $90.23\% \pm 5.29\%$ ; litter size:  $8.56 \pm 0.30$ ) (Fig. 2B, C). The severely subfertile phenotype was not due to abnormal mating behaviour because vaginal plugs were detected in all females mated with *Actrt1*-KO mice. We next performed in vitro fertilization using sperm collected from the cauda epididymis of *Actrt1*-KO and wild-type male mice. The percentage of two-cell embryos using sperm from *Actrt1*-KO mice ( $18.38\% \pm 1.50\%$ ) was significantly decreased compared with that using wild-type sperm ( $82.87\% \pm 1.96\%$ ) (Fig. 2D). Accordingly, we suggest that *Actrt1*-KO mice were severely subfertile due to a deficiency in fertilization.

#### **Aberrant head morphologies with acrosomal ultrastructural defects in *Actrt1*-KO sperm**

We next performed sperm analysis of *Actrt1*-KO mice. Sperm count ( $1.50 \times 10^6 \pm 0.03 \times 10^6$ ) and sperm motility ( $73.33\% \pm 3.28\%$ ) in *Actrt1*-KO mice showed no significant differences with respect to wild-type males (sperm count:  $1.63 \times 10^6 \pm 0.05 \times 10^6$ ; sperm motility:  $80.02\% \pm 2.31\%$ ) (Fig. 2E, F). Histological examination of the testis and epididymis revealed that the components in the seminiferous epithelium and sperm number in the caudal epididymis of *Actrt1*-KO mice were all similar to those of wild-type males (Fig. 2G). It is notable that deformed heads of elongated

spermatids (in testis) and sperm (in epididymis) could be observed under a high lens. We accordingly examined the morphology of sperm using Papanicolaou staining in detail (Fig. 3A; Fig. S2). In contrast to normal-appearing sperm from wild-type males, a higher ratio of sperm from *Actrt1*-KO mice showed deformed heads ( $58.71\% \pm 4.35\%$  vs.  $13.04\% \pm 0.79\%$ ) (Fig. 3B). Likewise, significantly more sperm with abnormal nuclear morphology were observed in *Actrt1*-KO mice ( $60.50\% \pm 2.16\%$ ) than in wild-type males ( $15.15\% \pm 0.63\%$ ), as observed by DAPI staining (Fig. S3A, B). Double staining of sperm using PNA-FITC (an acrosome dye) and MitoTracker red (a mitochondria dye) further revealed a disturbance of the typical crescent moon shape of the acrosome in *Actrt1*-KO mice (Fig. 3C). Notably, the ratio of acrosomes that were detached from the nucleus in *Actrt1*-KO sperm ( $39.74\% \pm 2.16\%$ ) was significantly higher than that in wild-type sperm ( $9.13\% \pm 1.44\%$ ) (Fig. 3D). TEM analysis further explored the phenomenon of acrosome detachment from the *Actrt1*-KO sperm nucleus (Fig. 3E; Fig. S4). The number of sperm with detached acrosomes was significantly increased in *Actrt1*-KO males ( $76.10\% \pm 2.78\%$ ) as compared with that in wild-type mice ( $13.16\% \pm 0.84\%$ ) (Fig. 3F). The ratio of detached acrosome in *Actrt1*-KO sperm as observed by TEM was higher than that identified by PNA-FITC staining, owing to the high resolution of TEM. Acroplaxome, an F-actin-containing plate between the acrosome and nucleus, is thought to be involved in acrosome-nuclear connection (Okō and Sutovsky, 2009). The distribution of the acroplaxome was disturbed, and sometimes it broke away from the nucleus in *Actrt1*-KO sperm (Fig. 3G). Moreover, the manchette of *Actrt1*-KO spermatids was largely disorganized (Fig. S3C). The manchette anomaly observed in *Actrt1*-KO spermatids may be a secondary effect of acrosome anomaly after the loss of ACTRT1 because manchette assembly depends on the stability of acrosome structure (Kierszenbaum et al., 2004).

### **ACTRT1 anchors developing acrosomes to the nucleus by interacting with IAM and NE proteins**

TEM analysis of the testis further revealed a loosened acroplaxome structure in *Actrt1*-KO spermatids at the cap/acrosome phase of acrosome formation (Fig. 4A). The ratio of spermatids with a loosened acroplaxome structure in *Actrt1*-KO spermatids ( $75.59\% \pm 1.82\%$ ) was much higher than that in wild-type spermatids ( $7.08\% \pm 1.07\%$ ) (Fig. 4B). The acroplaxome thickness that was measured in TEM images was significantly larger in *Actrt1*-KO spermatids ( $53.89 \text{ nm} \pm 2.23 \text{ nm}$ ) than in wild-type spermatids ( $23.11 \text{ nm} \pm 1.30 \text{ nm}$ ) (Fig. 4C). Moreover, the contents of PT-enriched proteins were analysed in sperm samples from wild-type and *Actrt1*-KO mice by Western blot. We found that the protein levels of ACTL7A and PLC $\zeta$  were significantly lower in *Actrt1*-KO sperm than in wild-type sperm. The protein contents of ACTRT2 and lamin A/C were significantly increased, whereas CAPZA3 and CAPZB expression was unchanged in sperm samples after ACTRT1 deletion (Fig. 4D). PLC $\zeta$  is a well-known sperm-borne oocyte activation factor (Hachem et al., 2017), and disruption of ACTL7A causes sperm fertilization failure due to reduced expression and abnormal localization of PLC $\zeta$  (Xin et al., 2020). The reduced ACTL7A and PLC $\zeta$  contents in sperm may partially explain the fertilization deficiency of *Actrt1*-KO male mice.

ACTRT1 may interact with IAM and NE proteins to anchor the developing acrosome to the nucleus. As immunoprecipitation-mass spectrometry (IP-MS) could not be performed due to the inability of commercial ACTRT1 antibodies to immunoprecipitate endogenous ACTRT1 protein, we chose a candidate-based approach by searching the literature for IAM and NE proteins whose knockout mice exhibit a deficiency of the IAM-acroplaxome-NE structure. Based on the similar phenotype with *Actrt1*-KO sperm, SPACA1, DPY19L2, FAM209, PARP11, and SPATA46 are candidate partners of ACTRT1. No close association of the IAM with the NE is formed in *Spaca1*-deficient spermatids (Fujihara et al., 2012), and importantly, the IAM protein SPACA1 could interact with ACTL7A to anchor the acrosome to the acroplaxome (Chen et al., 2021). DPY19L2 is the first NE protein

shown to be essential for anchoring the acrosome to the nucleus (Pierre et al., 2012). FAM209 colocalizes and interacts with DPY19L2 at the NE to maintain the developing acrosome (Castaneda et al., 2021). Both PARP11 and SPATA46 are NE proteins, and deficient spermatids exhibit structural defects in the NE associated with an abnormal nuclear shape (Meyer-Ficca et al., 2015; Chen et al., 2016). We found that Flag-tagged ACTRT1 was immunoprecipitated with Myc-tagged IAM protein SPACA1 in HEK293T cells (Fig. 5A). Myc-tagged ACTRT1 could be immunoprecipitated with the Flag-tagged NE proteins PARP11 and SPATA46, whereas no interactions existed between ACTRT1 and the NE proteins DPY19L2 and FAM209 in HEK293T cells (Fig. 5A). The interaction between the IAM protein SPACA1 and ACTRT1 was further confirmed by endogenous co-IP using mouse testis extracts (Fig. 5B). The endogenous interaction of ACTRT1 with the NE proteins PARP11 and SPATA46 was not detected because their commercial antibodies could not be applied for IP experiments. Moreover, loss of ACTRT1 did not affect the ACTL7A-ACTRT2 interaction but reduced the connection between ACTL7A and the IAM protein SPACA1 (Fig. 5C). The ACTL7A-SPACA1 interaction is known to anchor the acrosome to the acroplaxome (Chen et al., 2021). Collectively, we suggest that ACTRT1 within the sperm PT-specific ARP complex (ACTRT1-ACTRT2-ACTL7A-ACTL9) anchors developing acrosomes to the nucleus by connecting with the IAM protein SPACA1 and the NE proteins PARP11 and SPATA46 (Fig. 6).

## DISCUSSION

### Physiological roles of PT in spermiogenesis

One of the causes of male infertility is the abnormal development of spermatids into mature sperm. It is well known that the acrosome and flagella are responsible for oocyte fertilization and sperm motility, respectively. Correspondingly, globozoospermia (round-headed sperm without acrosome) and multiple



morphological anomalies of the sperm flagella (MMAF) are two types of asthenoteratozoospermia (Jiao et al., 2021). Our understanding of acrosome biogenesis and flagella formation originates from a large number of gene-deficient animal studies. In contrast, although the protein constituents of PT have been well studied during the last twenty years (Aul and Oko, 2002; Boeda et al., 2011; Hamilton et al., 2017; Heid et al., 2002; Herrada and Wolgemuth, 1997; Hess et al., 1993; Longo et al., 1987; Mujica et al., 2003; Oko and Morales, 1994; Olson and Winfrey, 1988; von Bulow et al., 1997), the physiological roles of PT remain largely unclear due to a lack of knockout/mutated mouse models. Among PT-enriched proteins, PLC $\zeta$ , PAWP, CAPZA3, ACTL7A, and ACTL9 have been investigated by loss-of-function studies in mice. Deletion of the *Plcz1* gene abolishes the ability of sperm to induce Ca<sup>2+</sup> oscillations in eggs (Hachem et al., 2017), whereas no abnormalities are observed in *Pawp*-KO mice (Satouh et al., 2015). *Capza3*-mutated mice show low sperm concentration, poor motility, and abnormally shaped sperm heads (Geyer et al., 2009). Disruption of *Actl7a* or *Actl9* causes acrosomal ultrastructural defects in sperm (Xin et al., 2020; Dai et al., 2021). In this study, we generated a novel mouse line lacking ACTRT1 and found a high ratio of detached acrosome and partial fertilization failure of *Actrt1*-KO sperm. Interestingly, the phenotype of *Actrt1*-KO males is quite similar to *Actl7a*- and *Actl9*-mutated mice, exhibiting detached acrosomes in sperm. The study of *Actl7a*-, *Actl9*-, and *Actrt1*-deficient sperm indicates a physiological role of PT in anchoring the developing acrosome to the nucleus. More knockout/mutated mouse models are still needed to comprehensively reveal the physiological roles of PT proteins in sperm biology.

### **Functions of the sperm PT-specific ARP complex**

Actin is one of the major components of the eukaryotic cytoskeleton. In addition to actin, eukaryotes also contain a conserved family of ARPs that have 17-45% sequence identity to actin. Several sperm PT-specific ARPs have been reported, including ACTRT1 (Heid et al., 2002), ACTRT2 (Heid et al., 2002), ACTRT3 (Hara et al., 2008), ACTL7A (Tanaka et al., 2003), ACTL7B (Chadwick et al., 1999), and ACTL9

(Dai et al., 2021). Two recent studies suggest that ACTL7A and ACTL9 form complexes and participate in acrosomal anchoring and egg activation (Dai et al., 2021; Xin et al., 2020). Chen et al. (Chen et al., 2021) further suggested an interaction between ACTL7A and the IAM protein SPACA1, explaining how ACTL7A anchors the acrosome to the acroplaxome. However, the mechanism underlying the anchoring of developing acrosomes to the NE is still largely unclear. ACTRT1 interacts with ACTRT2, ACTL7A, and ACTL9, as revealed by our co-IP analysis, suggesting an ARP complex in the sperm PT layer. More importantly, ACTRT1 could interact with the IAM protein SPACA1 and the NE proteins PARP11 and SPATA46 to mediate the connection between the acrosome and nucleus by the acroplaxome. However, whether the protein-protein interaction is direct or indirect needs further investigations. The phenotypes of *Actrt1*-KO, *Actl7a*-mutated, and *Actl9*-mutated mice show a high degree of similarity, including detachment of the acrosome, loosened acroplaxome structure, and sperm-derived fertilization failure. However, a defect in proacrosomal vesicle fusion shown in *Actl7a*- and *Actl9*-mutated spermatids was not observed in *Actrt1*-KO spermatids. It is unclear whether the fusion of proacrosomal vesicles into the acrosome is dependent on proper acroplaxome formation. Furthermore, *Actrt1*-KO mice showed partial fertilization failure whereas *Actl7a*- and *Actl9*-mutated mice exhibited total fertilization failure. We suggest a partial functional redundancy between ACTRT1 and ACTRT2 because i) these two proteins share over 70% similarity in nucleotide sequence; ii) ACTRT2 expression was increased in sperm samples from *Actrt1*-KO mice compared with those from control mice; and iii) ACTRT2 could also interact with ACTL7A, ACTL9, SPACA1, and PARP11 (Fig. S5). Generation and characterization of *Actrt1/2* double knockout mice will be helpful to examine whether functional redundancy truly exists between these two ARPs. The partial fertilization failure of *Actrt1*-KO mice may be explained by the reduced protein content of PLC $\zeta$  and ACTL7A in *Actrt1*-KO sperm because PLC $\zeta$  is a well-known sperm PT protein that induces Ca<sup>2+</sup> oscillations after entering oocytes (Escoffier et al., 2016; Hachem et al., 2017), and *Actl7a*-mutated sperm also fail to fertilize via ICSI (Xin et al., 2020). Although reduced expression and/or abnormal

localization of PLC $\zeta$  are observed in *Actl7a*-, *Actl9*-, and *Actrt1*-deficient sperm, the mechanisms underlying the regulation of PLC $\zeta$  by ACTL7A, ACTL9, and ACTRT1 are still unknown. These ARPs may influence the content and localization of PLC $\zeta$  in an indirect way.

### **Loss of ACTRT1 does not cause acephalic spermatozoa syndrome (ASS)**

While we were preparing our manuscript, Sha et al. reported two point mutations (c.95G>A and c.662A>G) of the *ACTRT1* gene in two ASS patients, and approximately 60% of sperm from *Actrt1*-KO mice were headless (Sha et al., 2021). Surprisingly, the phenotype observed in our *Actrt1*-KO mice was inconsistent with that in Sha's *Actrt1*-KO mice. There was no significant difference in the deletion strategy between these two KO mouse models because both adapted the C57BL/6 mouse strain and targeted the whole *Actrt1* gene (this gene has only one exon). However, we did not observe any ASS phenomenon in our *Actrt1*-KO mice; instead, detachment of the acrosome from the nucleus was identified in our mouse model. Headless sperm are actually 'pinhead sperm' because the unremoved cytoplasm and misarranged mitochondria attached to the top of the flagella are often mistakenly regarded as heads of reduced size (Baccetti et al., 1989; Le Lannou, 1979; Perotti and Gioria, 1981). *SPATA6* (Yuan et al., 2015), *SUN5* (Shang et al., 2017), *PMFBP1* (Zhu et al., 2018), and *CNTLN* (Zhang et al., 2021) are well-known ASS-related genes; indeed, residual cytoplasm and disordered mitochondria can be clearly observed at the fore-end of the flagella in their corresponding KO mice (Shang et al., 2017; Yuan et al., 2015; Zhang et al., 2021; Zhu et al., 2018). In Sha's *Actrt1*-KO sperm, the separated heads and tails are morphologically normal, and notably no cytoplasm or misarranged mitochondria attached to the top of the tails. The sperm head-to-tail coupling apparatus (HTCA) ensures sperm head-tail integrity, and defective HTCA is the basic cause of acephalic spermatozoa. ACTRT1 is a well-known PT protein surrounding the nuclei of sperm (Heid et al., 2002), and there is no evidence to indicate that ACTRT1 can regulate the HTCA structure. Data from independent laboratories (Chen et al., 2021; Dai et al., 2021), including ours (Figs. 1 and 5),

suggest that ACTRT1, ACTL7A, and ACTL9 form a large ARP complex and interact with the IAM protein SPACA1. The phenotype of our *Actrt1*-KO males (Figs. 3 and 4) was identical to that of *Actl7a*- and *Actl9*-mutated mice (Dai et al., 2021; Xin et al., 2020), showing a phenotype of acrosome detachment but not ASS. Many studies from independent laboratories support that mutations in *SUN5* and *PMFBP1* are the most common aetiologies of human ASS (Elkhatib et al., 2017; Liu et al., 2020; Shang et al., 2017; Zhu et al., 2018; Zhu et al., 2016). In contrast, the clinical evidence to link *ACTRT1* to human ASS is not strong enough because the consequences of a single-point mutation on ACTRT1 function have not been proven by any experiments. Accordingly, we suggest that *ACTRT1* is not considered a novel ASS-related gene at the current stage.

## MATERIALS AND METHODS

### Mouse model

Animal experiments were approved by the Animal Care and Use Committee of the College of Life Sciences, Beijing Normal University. The mouse *Actrt1* gene has 1 transcript (ENSMUST00000059466.2) and is located on chromosome X. The *Actrt1* gene has only one exon, and the whole *Actrt1* gene was selected as the knockout region. In brief, we selected two sgRNA primers with high scores (CRISPR finder: [https://www.sanger.ac.uk/htgt/wge/find\\_crisprs](https://www.sanger.ac.uk/htgt/wge/find_crisprs)) to generate a deletion of the whole *Actrt1* gene in mice (GRCm38). The wild-type genomic sequence is provided in Table S1, in which the *Actrt1* gene and the position of gRNAs are marked in red and blue, respectively. The sgRNAs (5'-CCATTGGTTGCTCAGTTCAA-3' and 5'-CTGGATAAGTAAAGTAACTC-3') were synthesized by Sangon Biotech (Shanghai, China). The two complementary DNA oligos of each sgRNA target were annealed (95 °C for 5 min and then naturally cooled to room temperature) and ligated to the pUC57-sgRNA plasmid (Cat# 51132, Addgene, USA) for cloning. The recombinant plasmid was transformed into DH5α competent cells, and the positive

clone was screened based on kanamycin resistance and sequencing. The recombinant plasmid was linearized and purified by phenol chloroform extraction. Transcriptions of the sgRNAs in vitro were performed using the MEGAshortscript Kit (Cat# AM1354, Ambion, USA) and purified using the MEGAclear Kit (Cat# AM1908, Ambion, USA). Cas9 mRNA was purchased from TriLink BioTechnologies (Cat# L-7206). Mouse zygotes were coinjected with an RNA mixture of Cas9 mRNA (50 ng/μl) and sgRNA (30 ng/μl). The injected zygotes were transferred into pseudopregnant recipients to obtain the F0 generation. DNA was extracted from tail tissues from 7-day-old offspring, and PCR amplification was carried out with genotyping primers (Table S2) using the Mouse Tissue Direct PCR Kit (Tiangen Biotech, Beijing, China) under the following conditions: 94 °C for 5 min; 35 cycles of 94 °C for 30 s, 61 °C for 30 s, and 72 °C for 30 s; and a final step of 72 °C for 5 min. PCR products were run on a 1% agarose gel in 1×TBE buffer and then subjected to sequencing (Sangon Biotech). A stable F1 generation (heterozygous mice) was obtained by mating positive F0 generation mice with wild-type C57BL/6JGpt mice.

### **RT-PCR**

Total RNA was extracted from mouse testes using an RNA Easy Fast Tissue/Cell Kit (Tiangen Biotech, Cat# DP451). First-strand cDNA synthesis and RT-PCR were performed using a FastKing One-Step RT-PCR Kit (Tiangen Biotech, Cat#KR123) according to the manufacturer's instructions. The amplification conditions for the RT-PCR were 5 min at 94 °C, followed by 35 cycles of 94 °C for 30 s, 62 °C for 30 s and 72 °C for 30 s, with a final five-minute extension at 72 °C. The primers for the specific recognition of *Actrt1* and *Actrt2* mRNA are listed in Table S3.

### **Expression plasmids and transient transfection**

Mouse *Actrt1* cDNA was chemically synthesized by GenScript Biotech Corporation (Suzhou, China) and inserted into Flag- or Myc-tagged pCMV vectors (Cat# D2632, D2672, Beyotime, Shanghai, China). Full-length cDNA encoding ACTRT2, ACTL7A, ACTL9, SPACA1, DPY19L2, FAM209, SPATA46, and PARP11 was

amplified by PCR using mouse testis cDNA as the template and cloned into Flag- or Myc-tagged pCMV vectors. The primers for plasmid construction are listed in Table S4. The construction of expression plasmids in this study was confirmed by sequencing (Sango Biotech, Shanghai, China). All sequencing results (.ab1 files) are provided in Supplementary Materials and can be viewed by Chromas software (<http://technelysium.com.au/wp/chromas/>). HEK293T cells (ATCC, Cat# CRL-11268) were cultured at 37 °C in a 5% CO<sub>2</sub> incubator (Panasonic/Sanyo CO<sub>2</sub> incubator MCO-18AIC) with Dulbecco's modified Eagle's medium (DMEM) (Thermo Fisher Scientific, Gibco™, Cat# 10569-044)+10% foetal bovine serum (FBS) (HyClone, Cat# 10099-141)+1% penicillin–streptomycin (Thermo Fisher Scientific, Gibco™, Cat# 15140-163). The transient transfection of HEK293T cells was performed by using Lipofectamine 3000 transfection reagent (Thermo Fisher Scientific, Invitrogen™, Cat# 11668-019) following the manufacturer's protocol (Thermo Fisher Scientific, CA, USA). Cells were then harvested 48 h after transfection.

### **Fertility testing**

To confirm the fertility of *Actrt1*-KO mice, natural mating tests were conducted. Briefly, three *Actrt1*-KO and three littermate control sexually mature male mice (8 to 12 weeks old) were paired with two 6~8-week-old C57BL/6J females (each male was mated with two female mice) for 2 months. The vaginal plugs of the mice were examined every morning. Then, the female mice with vaginal plugs were separately fed, and the number of pups per litter was recorded.

### **Histological analysis**

Testes and epididymis from adult male mice were dissected and fixed with 4% paraformaldehyde (PFA) (Beyotime, Shanghai, China, Cat# P0099) overnight at 4 °C. Fixed tissues were embedded in paraffin, sectioned (5 µm thick), dewaxed, and rehydrated. The sections were stained with H&E solution (Solarbio, Beijing, China, Cat# G1120) before imaging using an optical microscope (Leica Microsystems, Germany).

### **Assessment of sperm count and sperm motility**

The cauda epididymis was recovered, immersed in prewarmed HTF medium (Nanjing Aibei Biotechnology, Nanjing, China, Cat# M1130), and cut into several pieces to let sperm swim out at 37 °C in a 5% CO<sub>2</sub> humidified incubator for 15 min. Sperm counts were determined using a Fertility Counting Chamber (Makler, Haifa, Israel) under a light microscope, and sperm mobility was assessed via the application of a computer-assisted sperm analysis (CASA) system.

### **Sperm morphology**

Sperm were collected from the cauda epididymis and washed three times in PBS buffer. The sperm suspension was mounted on a glass slide, air-dried, and fixed with 4% PFA for 10 minutes at room temperature. The slides were stained with Papanicolaou solution (Solarbio, Cat# G2571) and observed using an optical microscope (Leica).

### **IVF in mice**

Eight-week-old C57BL/6J female mice were superovulated by injecting 5 IU (0.1 ml) of pregnant mare serum gonadotropin (PMSG) (Nanjing Aibei Biotechnology, Cat# M2620), followed by 5 IU (0.1 ml) of human chorionic gonadotropin (hCG) (Nanjing Aibei Biotechnology, Cat# M2520) 48 h later. The sperm was released from the cauda epididymis of 10-week-old male mice, and sperm capacitation was performed for 50 min using TYH solution (Nanjing Aibei Biotechnology, Cat# M2030). Cumulus-oocyte complexes (COCs) were obtained from the ampulla of the uterine tube at 14 hours after hCG injection. The ampulla was torn with a syringe needle, and the COCs were gently squeezed onto the liquid drops of HTF medium (Nanjing Aibei Biotechnology, Cat# M1130). COCs were then incubated with 5 to 10 µl sperm suspension (sperm concentration:  $1\sim5\times10^6$ ) in HTF liquid drops at 37 °C under 5% CO<sub>2</sub>. After 6 hours, the eggs were washed several times using HTF medium to remove the cumulus cells and then transferred to liquid drops of KSOM medium (Nanjing Aibei Biotechnology, Cat# M1430). Two-cell embryos were counted at 24 hours



postfertilization. All lipid drops were covered with mineral oil (Nanjing Aibei Biotechnology, Cat# ART-4008P) and equilibrated overnight at 37 °C under 5% CO<sub>2</sub>.

### **Immunofluorescence**

Spermatogenic cells were isolated from adult mouse testes by digestion with 1 mg/ml collagenase IV (Solarbio, Cat# G8160), 1 mg/ml hyaluronidase (Solarbio, Cat# H8030), 1 mg/ml trypsin (Solarbio, Cat# P7340), and 0.5 mg/ml DNase I (Solarbio, Cat# D8071) for 20 min on a shaker. A cell suspension containing spermatids was mounted on a glass slide, air-dried, and fixed with 4% PFA for 10 minutes at room temperature. After permeabilization with 1% Triton X-100 (Solarbio, Cat# P1080) for 30 min, the slides of sperm and spermatids were blocked with 5% goat serum (Solarbio, Cat# SL050) for 45 min. Anti-ACTRT1 antibody or anti-CTL7A antibody was added to the slide and incubated overnight at 4°C. After washing three times with PBS, Alexa Fluor 555-labelled donkey anti-rabbit IgG was incubated for 1 h at room temperature. For the staining of the acrosome, acroplaxomal, and manchette, PNA-FITC dye (Sigma–Aldrich, MO, USA, Cat# L7381), Actin-Tracker Red-555 dye (Beyotime, Cat# C2203), and Tubulin-Tracker Red dye (Beyotime, Cat# C1050) were used, respectively. For mitochondrial sheath staining, live sperm (before 4% PFA fixation) were stained with Mito Tracker Red (Beyotime). The nuclei were counterstained with DAPI dye (Beyotime, Cat# C1005).

### **Transmission electron microscopy (TEM)**

Precipitation of mouse sperm and testis tissues (~1 mm<sup>3</sup>) were fixed with 2.5% (vol/vol) glutaraldehyde in 0.1 M phosphate buffer (PB) (pH 7.4) for 24 hours at 4 °C. The samples were washed four times in PB and first immersed in 1% (wt/vol) OsO<sub>4</sub> and 1.5% (wt/vol) potassium ferricyanide aqueous solution at 4 °C for 2 h. After washing, the samples were dehydrated through graded alcohol (30%, 50%, 70%, 80%, 90%, 100%, 100%, 10 min each) into pure acetone (10 min twice). Samples were infiltrated in a graded mixture (3:1, 1:1, 1:3) of acetone and SPI-PON812 resin (21 ml SPO-PON812, 13 ml DDSA and 11 ml NMA), and then the pure resin was changed.



The specimens were embedded in pure resin with 1.5% BDMA and polymerized for 12 h at 45 °C, 48 h at 60 °C, cut into ultrathin sections (70 nm thick), and then stained with uranyl acetate and lead citrate for subsequent observation and photography with a Tecnai G2 Spirit 120 kV (FEI, Lausanne, Netherlands) electron microscope. All reagents were purchased from Zhongjingkeyi Technology (Beijing, China).

### **Immunoprecipitation (IP)**

Forty-eight hours after transfection, HEK293T cells were lysed with Pierce™ IP Lysis Buffer (Thermo Fisher, Cat# 87787) with protease inhibitor cocktail (MedChemExpress, Cat# HY-K0010) for 30 min at 4 °C and then centrifuged at 12,000 g for 10 min. Pierce IP Lysis Buffer was composed of 25 mM Tris-HCl pH 7.4, 150 mM NaCl, 1 mM EDTA, 1% NP-40 and 5% glycerol. To prepare Input samples, 30 µl protein lysates (~25 µg) were collected and boiled for 5 min in 1.2×SDS loading buffer (Beyotime, Cat# P0015). The lysates were precleared with 10 µl Pierce™ Protein A/G-conjugated Agarose (Thermo Fisher, Cat# 20422) for 1 h at 4 °C. Precleared lysates were incubated overnight with 2 µg anti-Myc antibody (Abmart, Cat#M20002) or anti-Flag antibody (Abmart, Cat# M20018) at 4 °C. The lysates were then incubated with 20 µl Pierce™ Protein A/G-conjugated Agarose for 2 h at 4 °C. The agarose beads were washed four times with Pierce™ IP Lysis Buffer and boiled for 5 min in 30 µl 1.2×SDS loading buffer. Input (~25 µg) and IP (~30 µl) samples were analysed by Western blotting by using anti-Flag or anti-Myc antibodies. For endogenous co-IP, adult mouse testis tissues were lysed with Pierce™ IP Lysis Buffer. Precleared lysates were separated into two groups: one group was treated with 2 µg anti-ACTL7A antibody (Proteintech, Cat# 17355-1-AP) or anti-SPACA1 antibody (Abcam, Cat# ab191843), and another group (negative control) was treated with 2 µg rabbit IgG (Beyotime, Cat# A7016). Other endogenous co-IP procedures were similar to the co-IP assay in HEK293T cells.

### **Subcellular structure protein extraction**

Protein extraction from different subcellular structures was performed according to the manufacturer's instructions (Sangon Biotech, Cat# C500073). Proteins are divided into four fractions containing cytosolic proteins, membrane and organelle proteins, nuclear proteins, and cytoskeletal filaments. Briefly, Extraction Buffer 1 was added to the cells and oscillated for ~10 min to lyse the cells. After centrifugation at 800 *g* for 10 min, the supernatant was collected as the cytosolic fraction. The pellet was resuspended in Extraction Buffer 2 and oscillated for ~30 min to solubilize membrane proteins. We collected the supernatant as a membranous fraction after another centrifugation step at 5000 *g* for 10 min. Extraction Buffer 3 was used for the solubilization of nuclear proteins under oscillation for ~30 min. Finally, the cytoskeletal proteins were pelleted at 6780 *g* for 10 min and completely dissolved in Extraction Buffer 4. Markers of cytosolic proteins (HSP90), membrane and organelle proteins (Calnexin), nuclear proteins (MLH1), and cytoskeletal filaments (Vimentin) were used to assess protein loading and fraction purity.

### **Western blot**

Proteins from HEK293T cells were extracted using RIPA lysis buffer (Applygen, Beijing, China, Cat# C1053) containing 1 mM PMSF and protease inhibitors (Applygen, Cat# C1055) on ice. For sperm samples, 1% SDS (Beyotime, Cat# ST628) was added to the RIPA lysis buffer. The supernatants were collected following centrifugation at 12,000 *g* for 20 min. We loaded 30 µg protein per lane. Proteins were electrophoresed in 10% SDS–PAGE gels (Beyotime, Cat# P0052A) and transferred to nitrocellulose membranes (GE Healthcare, WI, US). The blots were blocked in 5% milk (Beyotime, Cat# P0216) and incubated with the primary antibodies overnight at 4 °C, followed by incubation with anti-rabbit or mouse IgG H&L (HRP) (Abmart, Shanghai, China) at a 1/10,000 dilution for 1 hour. The signals were evaluated using the Super ECL Plus Western Blotting Substrate (Applygen, Cat# P1050) and a chemiluminescence imaging system (Tanon, Shanghai, China). The antibodies used in this study are listed in Table S5.

### Statistical analysis

Data were compared for statistical significance using GraphPad Prism version 5.01 (Graph Pad Software, San Diego, CA, USA). Student's *t test* was used for the statistical analyses. The data are presented as the mean±SEM, and differences were considered statistically significant at \* $p<0.05$ , \*\* $p<0.01$ , and \*\*\* $p<0.001$ .

**Abbreviations:** ARP, actin-related protein; ASS, acephalic spermatozoa syndrome; IAM, inner acrosomal membrane; IP, immunoprecipitation; IVF, in vitro fertilization; KO, knockout; NE, nuclear envelope; PT, perinuclear theca; TEM, transmission electron microscope.

### Acknowledgements

We would like to thank Dr. Liu Jin and Dr. Xi Chao from the Experimental Technology Center for Life Sciences, Beijing Normal University for technical assistance. We also acknowledge Dr. Li Xi-Xia and Lv Zhong-Shuang from the Center for Biological Imaging (CBI), Institute of Biophysics, Chinese Academy of Sciences for TEM analysis.

### Conflict of interests

The authors declare no conflict of interest.

### Author contributions

S.C. supervised the study and wrote the manuscript. X-Z.Z. and L.W. designed experiments and performed the molecular & biochemical experiments. S.C. performed animal experiments. H.J. and X-H.Z. contributed to the cell culture, plasmid construction, and animal breeding.

## Funding

This work was supported by the National Key Research and Development Project (2019YFA0802101), the Fundamental Research Funds for the Central Universities (2019NTST14), and the Open Fund of Key Laboratory of Cell Proliferation and Regulation Biology, Ministry of Education.

## References

**Aul, R.B. and Oko, R.J.** (2002). The major subacrosomal occupant of bull spermatozoa is a novel histone H2B variant associated with the forming acrosome during spermiogenesis. *Dev. Biol.* **242**, 376-387.

doi:10.1006/dbio.2002.0575

**Baccetti, B., Burrini, A.G., Collodel, G., Magnano, A.R., Piomboni, P., Renieri, T. and Sensini, C.** (1989). Morphogenesis of the decapitated and decaudated sperm defect in two brothers. *Gamete. Res.* **23**, 181-188.

doi:10.1002/mrd.1120230205

**Boeda, B., Knowles, P.P., Briggs, D.C., Murray-Rust, J., Soriano, E., Garvalov, B.K., McDonald, N.Q. and Way, M.** (2011). Molecular recognition of the Tes LIM2-3 domains by the actin-related protein Arp7A. *J. Biol. Chem.* **286**, 11543-11554.

doi:10.1074/jbc.M110.171264.

**Castaneda, J.M., Shimada, K., Satouh, Y., Yu, Z., Devlin, D.J., Ikawa, M. and Matzuk, M.M.** (2021). FAM209 associates with DPY19L2, and is required for sperm acrosome biogenesis and fertility in mice. *J. Cell. Sci.* **134**, jcs259206.

doi:10.1242/jcs.259206

**Chadwick, B.P., Mull, J., Helbling, L.A., Gill, S., Leyne, M., Robbins, C.M.,**

**Pinkett, H.W., Makalowska, I., Maayan, C., Blumenfeld, A. et al.** (1999). Cloning, mapping, and expression of two novel actin genes, actin-like-7A (ACTL7A) and actin-like-7B (ACTL7B), from the familial dysautonomia candidate region on 9q31. *Genomics*. **58**, 302-309.

doi:10.1006/geno.1999.5848

**Chen, J., Gu, Y., Zhang, Z., Zheng, W., Yang, L., Huang, W., Lin, S., Li, Y., Guo, H., Luo, M. et al.** (2016) Deficiency of SPATA46, a novel nuclear membrane protein, causes subfertility in male mice. *Biol. Reprod.* **95**, 58.

doi:10.1095/biolreprod.116.140996.

**Chen, P., Saiyin, H., Shi, R., Liu, B., Han, X., Gao, Y., Ye, X., Zhang, X. and Sun, Y.** (2021). Loss of SPACA1 function causes autosomal recessive globozoospermia by damaging the acrosome-acroplaxome complex. *Hum. Reprod.* **36**, 2587-2596.

doi:10.1093/humrep/deab144

**Dai, J., Zhang, T., Guo, J., Zhou, Q., Gu, Y., Zhang, J., Hu, L., Zong, Y., Song, J., Zhang, S. et al.** (2021). Homozygous pathogenic variants in ACTL9 cause fertilization failure and male infertility in humans and mice. *Am. J. Hum. Genet.* **108**, 469-481.

doi:10.1016/j.ajhg.2021.02.004

**Elkhatib, R.A., Paci, M., Longepied, G., Saias-Magnan, J., Courbiere, B., Guichaoua, M.R., Levy, N., Metzler-Guillemain, C. and Mitchell, M.J.** (2017). Homozygous deletion of SUN5 in three men with decapitated spermatozoa. *Hum. Mol. Genet.* **26**, 3167-3171.

doi:10.1093/hmg/ddx200

**Escoffier, J., Lee, H.C., Yassine, S., Zouari, R., Martinez, G., Karaouzene, T., Coutton, C., Kherraf, Z.E., Halouani, L., Triki, C. et al.** (2016). Homozygous mutation of PLCZ1 leads to defective human oocyte activation and infertility that is not rescued by the WW-binding protein PAWP. *Hum. Mol. Genet.* **25**, 878-891.

doi:10.1093/hmg/ddv617

**Fujihara, Y., Satouh, Y., Inoue, N., Isotani, A., Ikawa, M. and Okabe, M.** (2012). SPACA1-deficient male mice are infertile with abnormally shaped sperm heads reminiscent of globozoospermia. *Development*. **139**, 3583-3589.

doi:10.1242/dev.081778

**Geyer, C.B., Inselman, A.L., Sunman, J.A., Bornstein, S., Handel, M.A. and Eddy, E.M.** (2009). A missense mutation in the Capza3 gene and disruption of F-actin organization in spermatids of repro32 infertile male mice. *Dev. Biol.* **330**, 142-152.

doi:10.1242/dev.081778

**Hachem, A., Godwin, J., Ruas, M., Lee, H.C., Ferrer Buitrago, M., Ardestani, G., Bassett, A., Fox, S., Navarrete, F., de Sutter, P. et al.** (2017). PLC $\zeta$  is the physiological trigger of the Ca<sup>2+</sup> oscillations that induce embryogenesis in mammals but conception can occur in its absence. *Development*. **144**, 2914-2924.

doi:10.1242/dev.150227

**Hamilton, L.E., Acteau, G., Xu, W., Sutovsky, P. and Oko, R.** (2017). The developmental origin and compartmentalization of glutathione-s-transferase omega 2 isoforms in the perinuclear theca of eutherian spermatozoa. *Biol. Reprod.* **97**, 612-621.

doi:10.1093/biolre/iox122

**Hamilton, L.E., Suzuki, J., Acteau, G., Shi, M., Xu, W., Meinsohn, M.C., Sutovsky, P. and Oko, R.** (2018). WBP2 shares a common location in mouse spermatozoa with WBP2NL/PAWP and like its descendent is a candidate mouse oocyte-activating factor. *Biol. Reprod.* **99**, 1171-1183.

doi:10.1093/biolre/ioy156

**Hara, Y., Yamagata, K., Oguchi, K. and Baba, T.** (2008). Nuclear localization of profilin III-ArpM1 complex in mouse spermiogenesis. *FEBS. Lett.* **582**, 2998-3004.

doi:10.1016/j.febslet.2008.07.058

**Heid, H., Figge, U., Winter, S., Kuhn, C., Zimbelmann, R., Franke, W.** (2002). Novel actin-related proteins Arp-T1 and Arp-T2 as components of the cytoskeletal calyx of the mammalian sperm head. *Exp. Cell. Res.* **279**, 177-187.

doi:10.1006/excr.2002.5603

**Herrada, G. and Wolgemuth, D.J.** (1997). The mouse transcription factor Stat4 is expressed in haploid male germ cells and is present in the perinuclear theca of spermatozoa. *J. Cell. Sci.* **110**, 1543-1553.

doi:10.1242/jcs.110.14.1543

**Hess, H., Heid, H. and Franke, W.W.** (1993). Molecular characterization of mammalian cylicin, a basic protein of the sperm head cytoskeleton. *J. Cell. Biol.* **122**, 1043-1052.

doi:10.1083/jcb.122.5.104

**Hess, H., Heid, H., Zimbelmann, R. and Franke, W.W.** (1995). The protein complexity of the cytoskeleton of bovine and human sperm heads: the identification and characterization of cylicin II. *Exp. Cell. Res.* **218**, 174-182.

doi:10.1006/excr.1995.1145

**Jiao, S.Y., Yang, Y.H. and Chen, S.R.** (2021). Molecular genetics of infertility: loss-of-function mutations in humans and corresponding knockout/mutated mice. *Hum. Reprod. Update.* **27**, 154-189.

doi:10.1093/humupd/dmaa034

**Kierszenbaum, A.L. and Tres, L.L.** (2004). The acrosome-acroplaxome-manchette complex and the shaping of the spermatid head. *Arch. Histol. Cytol.* **67**:271-284.

doi:10.1679/aohc.67.271

**Le Lannou, D.** (1979). Teratospermia consisting of the absence of the head of the spermatozoa because of a fault in the joint between the head and the neck of the sperm in man. *J. Gynecol. Obstet. Biol. Reprod.* **8**:43-45.

**Lécuyer, C., Dacheux, J.L., Hermand, E., Mazeman, E., Rousseaux, J. and Rousseaux-Prévost, R.** (2000) Actin-binding properties and colocalization with actin during spermiogenesis of mammalian sperm calicin. *Biol. Reprod.* **63**, 1801-1810.

doi:10.1095/biolreprod63.6.1801

**Liu, G., Wang, N., Zhang, H., Yin, S., Dai, H., Lin, G. and Li, W.** (2020). Novel mutations in PMFBP1, TSGA10 and SUN5: expanding the spectrum of mutations that may cause acephalic spermatozoa. *Clin. Genet.* **97**, 938-939.

doi:10.1111/cge.13747

**Longo, F.J., Krohne, G. and Franke, W.W.** (1987). Basic proteins of the perinuclear theca of mammalian spermatozoa and spermatids: a novel class of cytoskeletal elements. *J. Cell. Biol.* **105**, 1105-1120.

doi:10.1083/jcb.105.3.1105

**Meyer-Ficca, M.L., Ihara, M., Bader, J.J., Leu, N.A., Beneke, S. and Meyer, R.G.** (2015). Spermatid head elongation with normal nuclear shaping requires ADP-ribosyltransferase PARP11 (ARTD11) in mice. *Biol. Reprod.* **92**, 80.

doi:10.1095/biolreprod.114.123661

**Mujica, A., Navarro-Garcia, F., Hernandez-Gonzalez, E.O. and De Lourdes Juarez-Mosqueda, M.** (2003). Perinuclear theca during spermatozoa maturation leading to fertilization. *Microsc. Res. Tech.* **61**, 76-87.

doi:10.1002/jemt.10318

Oh, S.D., Park, S.Y., Park, J.I., Chun, S.Y., Ryu, T.H. and Soh, J. (2013). The novel, actin-like protein Tact3 is expressed in rodent testicular haploid germ cells. *Mol. Reprod. Dev.* **80**, 988-999.

doi:10.1002/mrd.22262

**Oko, R. and Morales, C.R.** (1994). A novel testicular protein, with sequence similarities to a family of lipid binding proteins, is a major component of the rat sperm perinuclear theca. *Dev. Biol.* **166**, 235-245.

doi:10.1006/dbio.1994.1310

**Oko, R. and Sutovsky, P.** (2009). Biogenesis of sperm perinuclear theca and its role in sperm functional competence and fertilization. *J Reprod Immunol.* **83**, 2-7.

doi:10.1016/j.jri.2009.05.008

**Olson, G.E. and Winfrey, V.P.** (1988). Characterization of the postacrosomal sheath of bovine spermatozoa. *Gamete. Res.* **20**, 329-342.

doi:10.1002/mrd.1120200308

**Perotti, M.E. and Gioria, M.** (1981). Fine structure and morphogenesis of "headless" human spermatozoa associated with infertility. *Cell. Biol. Int. Rep.* **5**, 113.

doi:10.1016/0309-1651(81)90018-7



**Pierre, V., Martinez, G., Coutton, C., Delaroche, J., Yassine, S., Novella, C., Pernet-Gallay, K., Hennebicq, S., Ray, P.F. and Arnoult, C.** (2012). Absence of Dpy19l2, a new inner nuclear membrane protein, causes globozoospermia in mice by preventing the anchoring of the acrosome to the nucleus. *Development*. **139**, 2955-2965.

doi: 10.1242/dev.077982

**Satouh, Y., Nozawa, K. and Ikawa, M.** (2015). Sperm postacrosomal WW domain-binding protein is not required for mouse egg activation. *Biol. Reprod.* **93**, 94.

doi:10.1095/biolreprod.115.131441

**Sha, Y., Liu, W., Li, L., Serafimovski, M., Isachenko, V., Li, Y., Chen, J., Zhao, B., Wang, Y. and Wei, X.** (2021). Pathogenic variants in ACTRT1 cause acephalic spermatozoa syndrome. *Front. Cell. Dev. Biol.* **9**, 676246.

doi:10.3389/fcell.2021.676246

**Shang, Y., Zhu, F., Wang, L., Ouyang, Y.C., Dong, M.Z., Liu, C., Zhao, H., Cui, X., Ma, D. and Zhang, Z. et al.** (2017). Essential role for SUN5 in anchoring sperm head to the tail. *eLife*. **6**, e28199.

doi:10.7554/eLife.28199

**Tanaka, H., Iguchi, N., Egydio de Carvalho, C., Tadokoro, Y., Yomogida, K. and Nishimune, Y.** (2003). Novel actin-like proteins T-ACTIN 1 and T-ACTIN 2 are differentially expressed in the cytoplasm and nucleus of mouse haploid germ cells. *Biol. Reprod.* **69**, 475-482.

doi:10.1095/biolreprod.103.015867

**von Bulow, M., Rackwitz, H.R., Zimbelmann, R. and Franke, W.W.** (1997). CP beta3, a novel isoform of an actin-binding protein, is a component of the cytoskeletal calyx of the mammalian sperm head. *Exp. Cell. Res.* **233**, 216-224.

doi:10.1006/excr.1997.3564

**Wu, A.T., Sutovsky, P., Manandhar, G., Xu, W., Katayama, M., Day, B.N., Park, K.W., Yi, Y.J., Xi, Y.W. and Prather, R.S. et al. (2007).** PAWP, a sperm-specific WW domain-binding protein, promotes meiotic resumption and pronuclear development during fertilization. *J. Biol. Chem.* **282**, 12164-12175.

doi:10.1074/jbc.M609132200

**Xin, A., Qu, R., Chen, G., Zhang, L., Chen, J., Tao, C., Fu, J., Tang, J., Ru, Y. and Chen, Y. et al. (2020).** Disruption in ACTL7A causes acrosomal ultrastructural defects in human and mouse sperm as a novel male factor inducing early embryonic arrest. *Sci. Adv.* **6**, eaaz4796.

doi:10.1126/sciadv.aaz4796

**Yuan, S., Stratton, C.J., Bao, J., Zheng, H., Bhetwal, B.P., Yanagimachi, R. and Yan, W. (2015).** Spata6 is required for normal assembly of the sperm connecting piece and tight head-tail conjunction. *Proc. Natl. Acad. Sci. U. S. A.* **112**, E430-439.

doi:10.1073/pnas.1424648112

**Zhang, Y., Liu, C., Wu, B., Li, L., Li, W. and Yuan, L. (2021).** The missing linker between SUN5 and PMFBP1 in sperm head-tail coupling apparatus. *Nat Commun.* **12**, 4926.

doi:10.1038/s41467-021-25227-w

**Zhu, F., Liu, C., Wang, F., Yang, X., Zhang, J., Wu, H., Zhang, Z., He, X., Zhang, Z. and Zhou, P. et al. (2018).** Mutations in PMFBP1 cause acephalic spermatozoa syndrome. *Am. J. Hum. Genet.* **103**, 188-199.

doi:10.1016/j.ajhg.2018.06.010

**Zhu, F., Wang, F., Yang, X., Zhang, J., Wu, H., Zhang, Z., Zhang, Z., He, X., Zhou, P. and Wei, Z. et al. (2016).** Biallelic SUN5 mutations cause autosomal-recessive acephalic spermatozoa syndrome. *Am. J. Hum. Genet.* **99**, 942-949.

doi:10.1016/j.ajhg.2016.08.004

## Figures

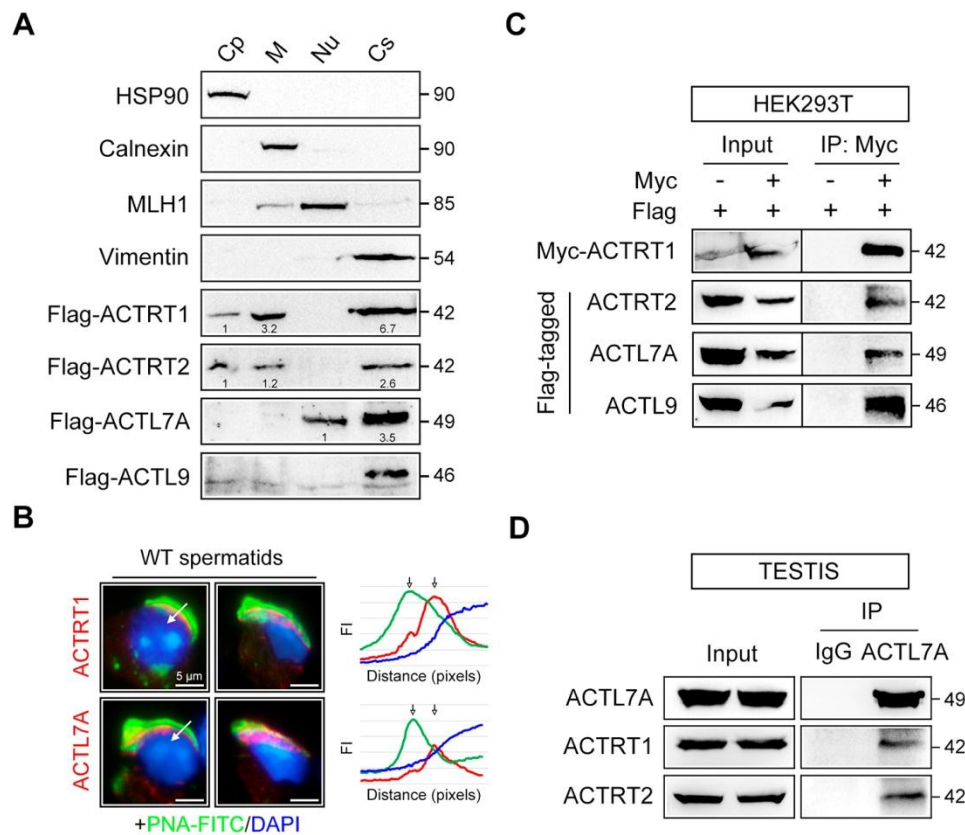


**Fig. 1. Organization of ACTRT1, ACTRT2, ACTL7A, and ACTL9 as an ARP complex.** (A) Different protein components of Flag-tagged ACTRT1-, ACTRT2-, ACTL7A-, or ACTL9-transfected HEK293T cells were isolated using a Subcellular Structure Protein Extraction Kit (Sango Biotech). The cytoplasmic marker heat-shock protein 90 (HSP90), the membrane marker calnexin, the nuclear marker mutL homologue 1 (MLH1), and the cytoskeleton marker vimentin were used to assess fraction purity. Flag-tagged ACTRT1, ACTRT2, ACTL7A, and ACTL9 were mainly distributed in the cytoskeleton. Cp, cytosolic proteins; M, membrane proteins; Nu, nuclear proteins; Cs, cytoskeletal filaments. (B) Localization of ACTRT1 and ACTL7A in round and elongated spermatids. Isolated spermatogenic cells were immunostained for ACTRT1 or ACTL7A (red). Cells were counterstained with the acrosome dye PNA-FITC (green) and the nuclear dye DAPI (blue). Scale bar, 5  $\mu$ m. The pixel overlaps of ACTRT1 or ACTL7A (red) and PNA-FITC (green) were

analysed using ImageJ software (<https://imagej.nih.gov/ij/>). FI, fluorescence intensity.

(C) A coimmunoprecipitation (co-IP) assay indicated that Myc-tagged ACTRT1 interacted with Flag-tagged ACTRT2, ACTL7A, and ACTL9 in HEK293T cells. Myc antibody was utilized to immunoprecipitate Myc-tagged ACTRT1. For the negative control group, Flag-tagged ACTRT2, ACTL7A, or ACTL9 was transfected into HEK293T cells; for the IP group, Myc-tagged ACTRT1 and Flag-tagged ACTRT2, ACTL7A, or ACTL9 were cotransfected into HEK293T cells. (D) Endogenous ACTL7A was coimmunoprecipitated with endogenous ACTRT1 and ACTRT2. Mouse testis lysates were immunoprecipitated with anti-ACTL7A antibody. For the negative control group, rabbit IgG was utilized instead of anti-ACTL7A antibody. The precipitates were subjected to immunoblotting with antibodies against ACTRT1 and ACTRT2.

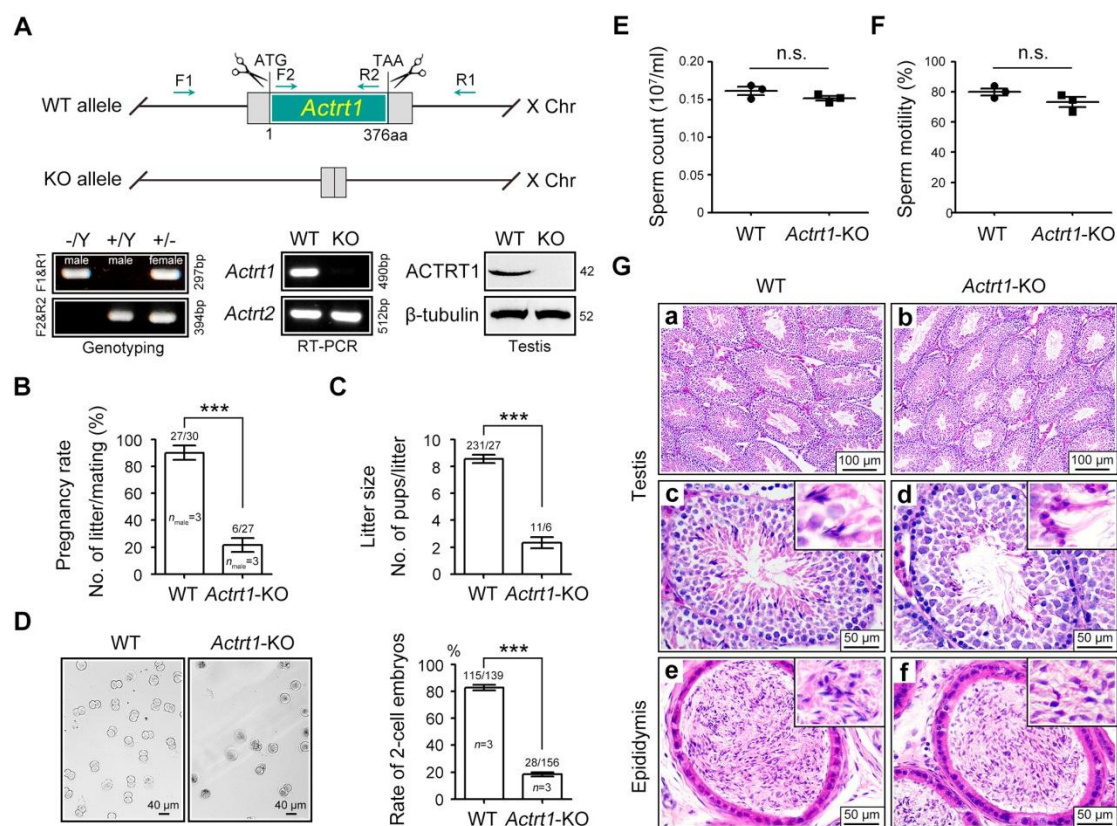


**Fig. 2. *Actrt1*-KO male mice are severely subfertile due to fertilization failure.** (A) Schematic diagram of the generation of *Actrt1*-KO mice using CRISPR/Cas9. The detailed procedure for the generation of *Actrt1*-KO mice is provided in the Methods. As the *Actrt1* gene is located on chromosome X, *Actrt1*<sup>+/-</sup> female mice were mated with wild-type males to generate *Actrt1*<sup>-Y</sup> (*Actrt1*-KO) mice after genotyping PCR. RT-PCR and Western blotting were used to detect the knockout efficiency of ACTRT1 in the testis at the mRNA and protein levels, respectively.  $\beta$ -tubulin served as a loading control. Biologically independent mice were examined in three separate experiments with similar results. (B, C) Fertility assessment experiments were performed in three *Actrt1*-KO male mice and three littermate WT male mice for 2 months. Each male mouse was mated with two C57BL/6J female mice. Vaginal plugs were observed in all mated females, and the number of pups per litter was recorded. Of the 30 female mice mated with WT males, 27 were pregnant and gave rise to 231 offspring. In contrast, of the 27 female mice mated with *Actrt1*-KO males, only 6 were pregnant and gave rise to 11 offspring. (D) An in vitro fertilization assay was

performed using sperm from *Actrt1*-KO and control male mice ( $n=3$  for each group). The rate of two-cell embryos was calculated at 24 hours postfertilization. Scale bars, 40  $\mu\text{m}$ . (E, F) Sperm counts were determined using a fertility counting chamber (Makler) under a light microscope (E), and sperm motility was assessed via the application of a CASA system (F). Data in B-F are presented as the means  $\pm$  SEM. Student's *t* test. \*\*\* $p<0.001$ ; n.s., not significant. (G) H&E staining of paraffin-embedded tissue sections of testes and epididymis. Scale bars, 50 or 100  $\mu\text{m}$ .

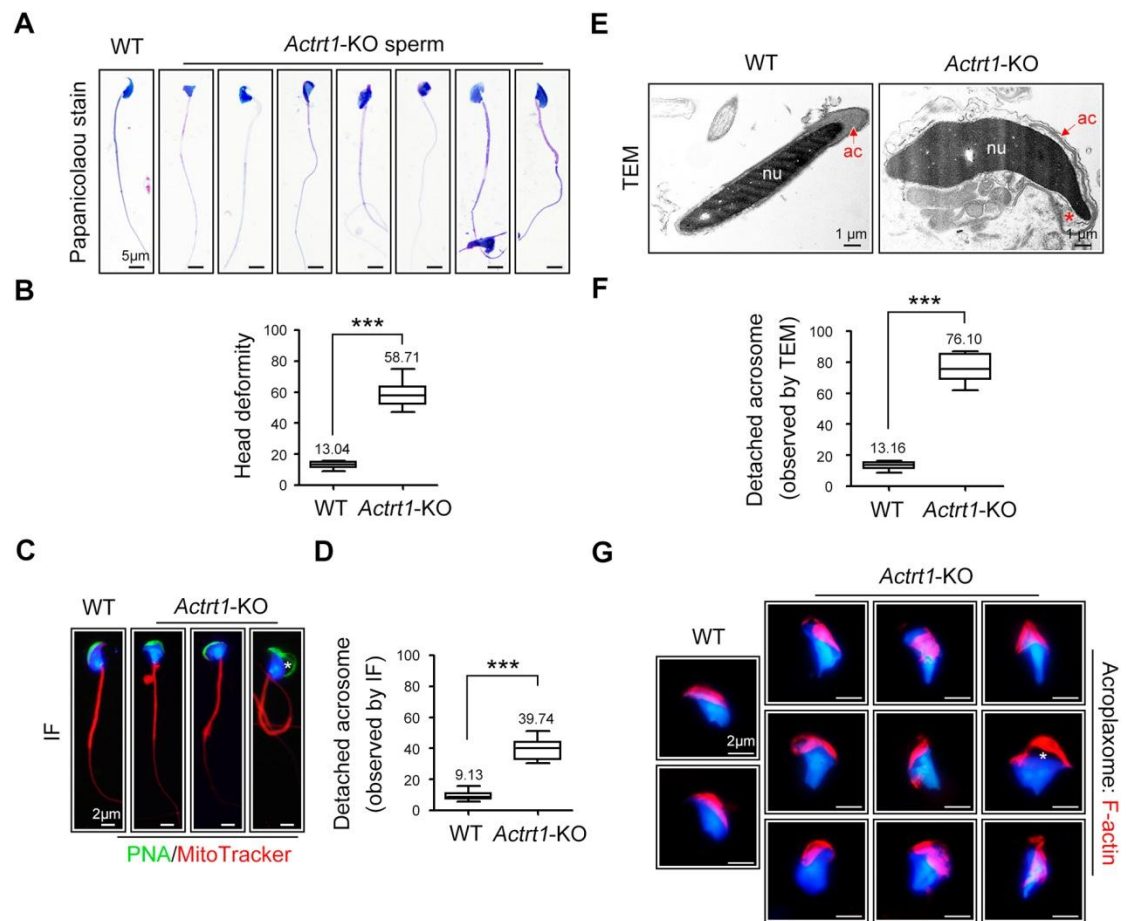


**Fig. 3. Malformed head shape with detached acrosome of *Actrt1*-KO sperm.** (A) Light microscopy analysis of sperm from control and *Actrt1*-KO mice with Papanicolaou staining. Scale bars, 5  $\mu$ m. (B) The ratio of head deformity in Papanicolaou-stained sperm. (C) Visualization of the acrosome and mitochondrial sheath using the fluorescent dye PNA-FITC and MitoTracker Red, respectively. Stars indicate the detachment of the acrosome. Scale bars, 2  $\mu$ m. (D) Percentage of sperm with the detached acrosome as revealed by PNA-FITC staining. (E) TEM analysis revealed detachment of the acrosome (ac, red arrows) from the sperm nuclei (nu) in *Actrt1*-KO sperm. Stars indicate the enlarged space between the acrosome and nucleus. Scale bars, 1  $\mu$ m. (F) Percentage of sperm with detached acrosomes in wild-type and *Actrt1*-KO mice as revealed by TEM. (G) Acroplaxome actin bundles of spermatids were visible by F-actin-Tracker Red staining. The distribution of the F-actin-enriched acroplaxome was largely disorganized in *Actrt1*-KO sperm. Stars

indicate the detachment of the acroplaxome from the nucleus. Scale bars, 2  $\mu\text{m}$ . Data in B, D, and F are presented as the means  $\pm$  SEM.  $n=3$  mice for each group. Student's *t test*. \*\*\* $p<0.001$ . At least 100 sperm were counted in each experiment.



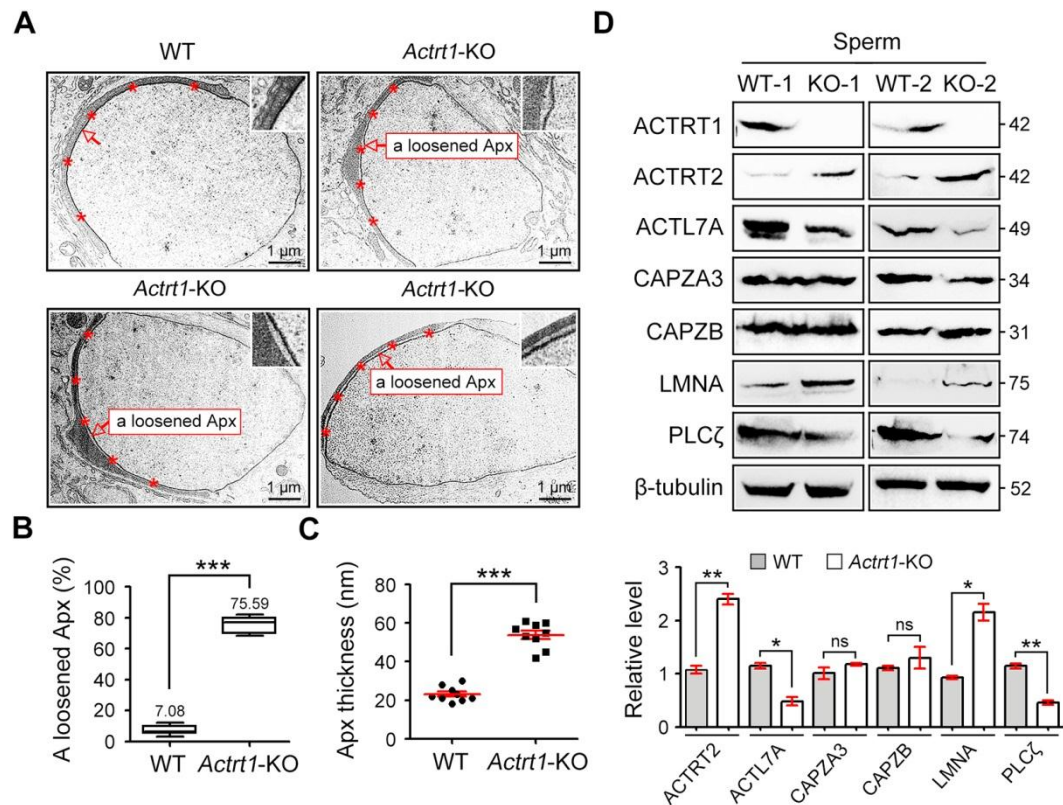


**Fig. 4. A loosened acroplaxome structure in *Actrt1*-KO spermatids.** (A) The acroplaxome is localized between the acrosome and nuclear envelope. TEM analysis of testis tissues revealed a loosened acroplaxome structure (red arrows) of *Actrt1*-KO spermatids at the cap/acrosome phase of acrosome formation. Scale bars, 1  $\mu$ m. Apx, acroplaxome. (B) Percentage of spermatids with a loosened acroplaxome structure in control and *Actrt1*-KO testes as revealed in the TEM images. (C) Five sites of the acroplaxome in a spermatid were randomly selected (stars indicated in A). The thickness of the acroplaxome structure in the TEM images at a magnification of 30,000x was measured and averaged. Data in B and C are presented as the means  $\pm$  SEM.  $n=3$  mice for each group. Student's  $t$  test. \*\*\* $p<0.001$ . At least 50 spermatids were counted in each experiment. (D) The protein levels of PT-specific proteins ACTRT2, ACTL7A, CAPZA3, CAPZB, Lamin A/C (LMNA), and PLC $\zeta$  in wild-type and *Actrt1*-KO sperm. To extract proteins from sperm samples, 1% SDS was added to RIPA lysis buffer.  $\beta$ -tubulin served as an internal control. Bar graphs representing

band intensities of the blot, and data represent the mean  $\pm$  SEM of two biological replicates. Student's *t test*, \* $p<0.05$ , \*\* $p<0.01$ , ns: no significance.

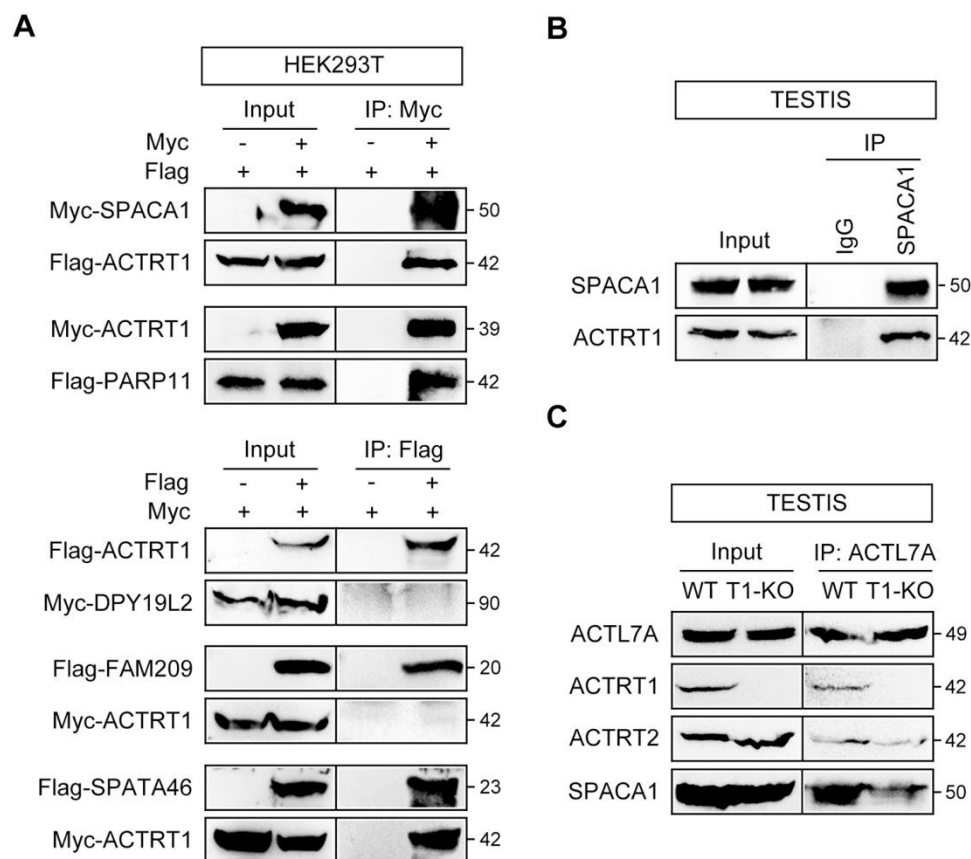


**Fig. 5. ACTRT1 interacts with IAM and NE proteins to anchor the acrosome to the nucleus.** (A) Flag- and/or Myc-tagged proteins were transfected into HEK293T cells. Protein lysates were immunoprecipitated with anti-Flag antibody or anti-Myc antibody and then detected with the corresponding tag antibody by SDS-PAGE. Co-IP assays indicated that ACTRT1 was immunoprecipitated with SPACA1, PARP11, and SPATA46 in HEK293T cell extracts. (B) Mouse testis lysates were immunoprecipitated with anti-SPACA1 antibody (Abcam, Cat#ab191843) and then detected with anti-ACTRT1 antibody. Rabbit IgG served as the negative control. An interaction exists between endogenous ACTRT1 and SPACA1. (C) Testis lysates from wild-type and *Actrt1*-KO mice were immunoprecipitated with anti-ACTL7A antibody (Proteintech, Cat# 17355-1-AP) and then detected with anti-ACTRT1, anti-ACTRT2, and anti-SPACA1 antibodies. Loss of ACTRT1 did not affect the co-IP of ACTRT2 and ACTL7A but weakened the interaction between ACTL7A and SPACA1.

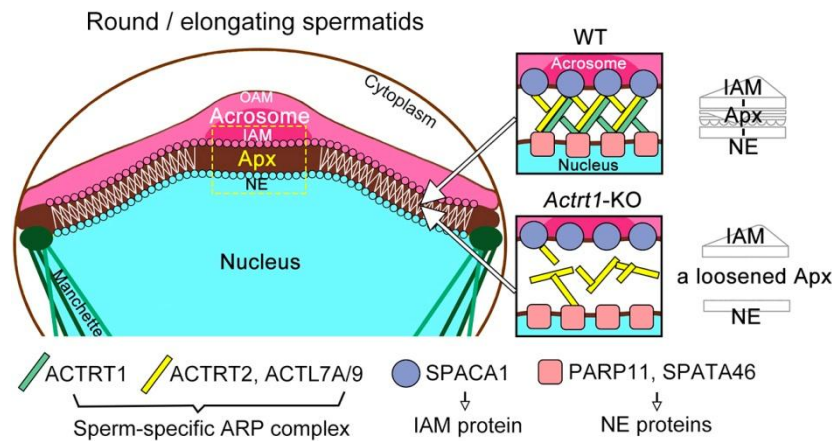


**Fig. 6. A proposed model for the role of ACTRT1 in the integration of acrosome to the nucleus.** ACTRT1 interacts with ACTRT2, ACTL7A, and ACTL9, forming an ARP protein complex in the acroplaxome. ACTRT1 further connects with the IAM protein SPACA1 and the NE proteins PARP11 and SPATA46. Loss of ACTRT1 leads to a loosened acroplaxome structure of spermatids, and the developing acrosome is easily detached from the nucleus. IAM, inner acrosomal membrane; NE, nuclear envelope; Apx, acroplaxome.

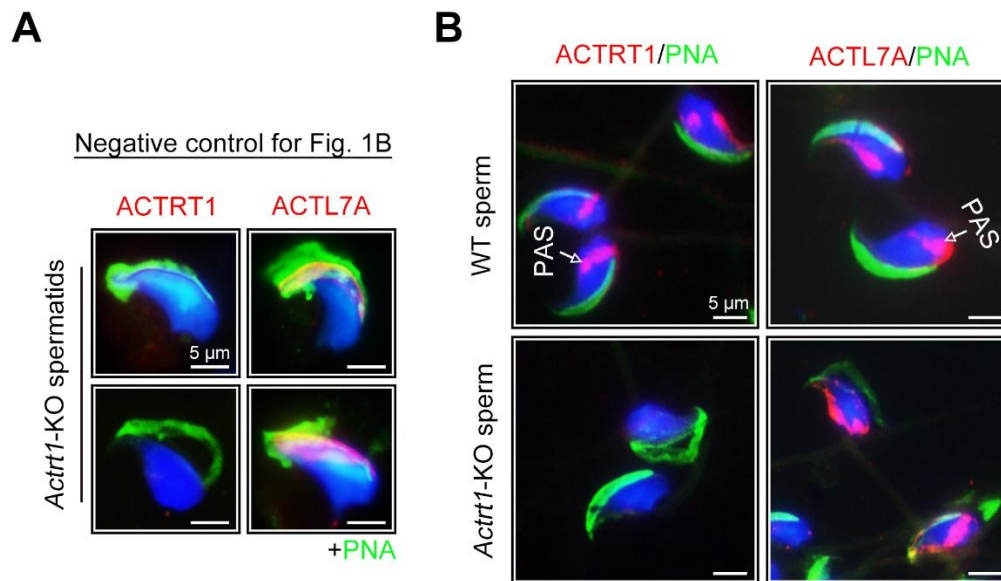


**Fig. S1. Localization of ACTRT1 and ACTL7A in spermatids/spermatozoa.** (A) The negative control for Fig. 1B. Immunofluorescent staining of ACTRT1 and ACTL7A (red) in *Actrt1*-KO testicular spermatids. The signal of ACTRT1 was lost whereas the subacrosomal localization of ACTL7A was unaltered in *Actrt1*-KO spermatids. (B) The sperm smear from WT and *Actrt1*-KO mice was immunostained for ACTRT1 or ACTL7A (red). In mature spermatozoa, ACTRT1 and ACTL7A translocated from the subacrosomal region to the postacrosomal sheath (PAS). Sections were counterstained with the acrosome dye PNA-FITC (green) and the nuclear dye DAPI (blue). Scale bar, 5  $\mu$ m.

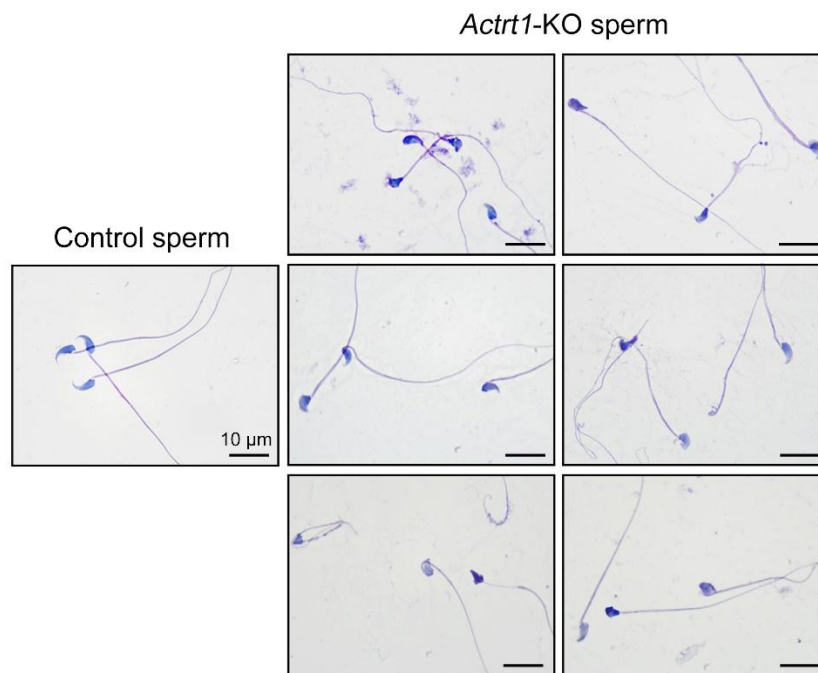


**Fig. S2. Light microscopy of *Actrt1*-KO sperm.** Sperm of wild-type and *Actrt1*-KO mice were stained by the Papanicolaou technique. A high ratio of sperm with deformed heads was observed in *Actrt1*-KO sperm. Scale bars, 10  $\mu$ m.

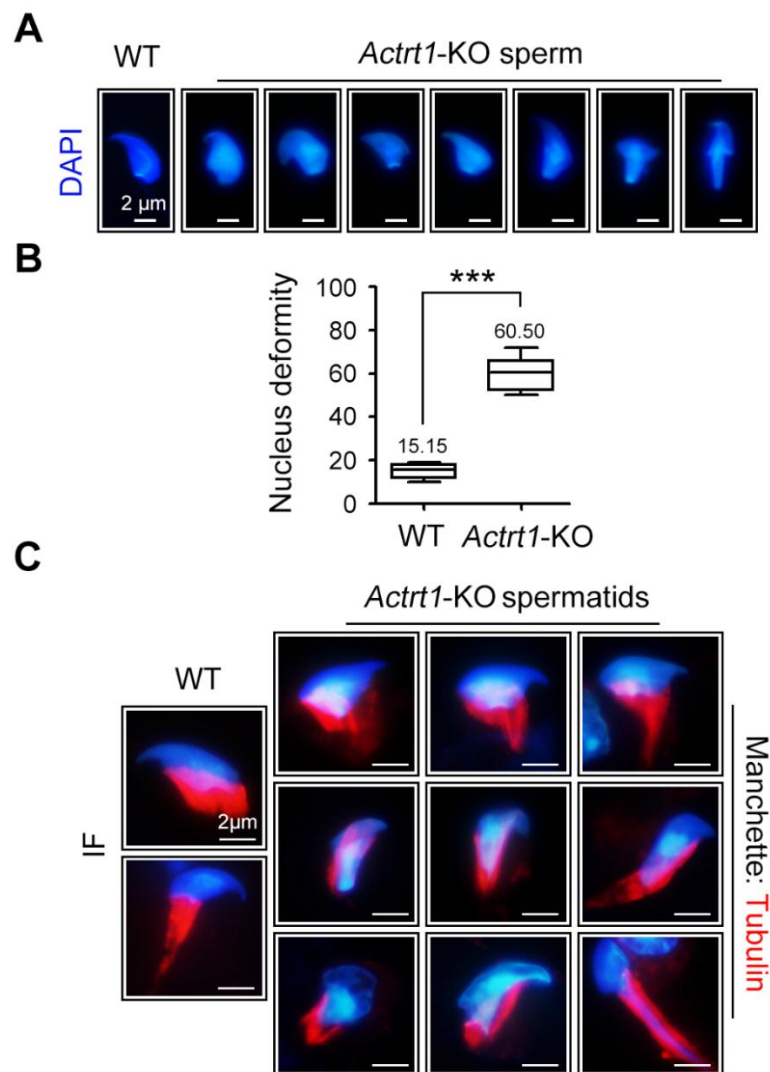


**Fig. S3. Nucleus deformity and abnormal development of manchette in *Actrt1*-KO sperm.** (A) Representative images of DAPI-stained nucleus of wild-type and *Actrt1*-KO sperm. Scale bars, 2  $\mu$ m. (B) The percentage of nucleus deformity in DAPI-stained wild-type and *Actrt1*-KO sperm. Data are presented as the means $\pm$ SEM.  $n=3$  mice for each group. Student's  $t$  test. \*\*\* $p<0.001$ . At least 50 sperm were counted in each experiment. (C) The manchette of spermatids from wild-type and *Actrt1*-KO mice was observed by the staining of Tubulin-Tracker Red. Nucleus were counterstained with DAPI. Scale bars, 2  $\mu$ m.



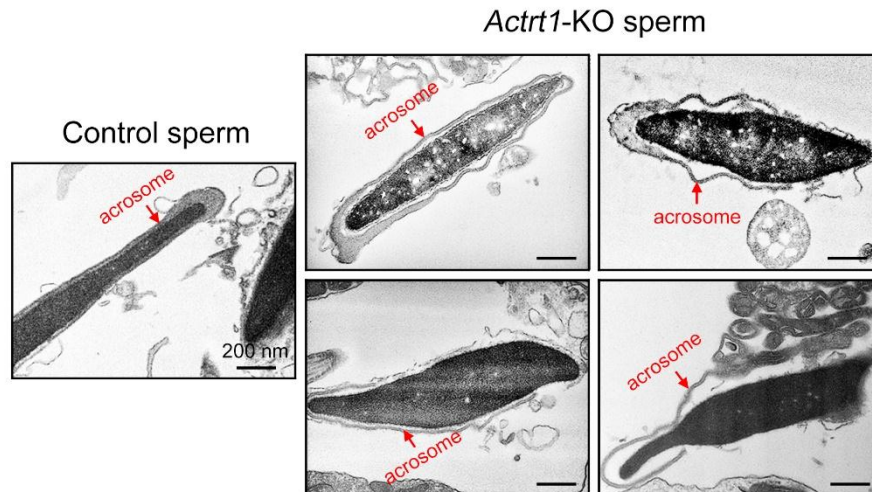


**Fig. S4. TEM analysis of *Actrt1*-KO sperm.** TEM analysis revealed the detachment of the acrosome from the nucleus in the *Actrt1*-KO sperm. The acrosomes were indicated by arrows in figures. Scale bars, 200 nm.



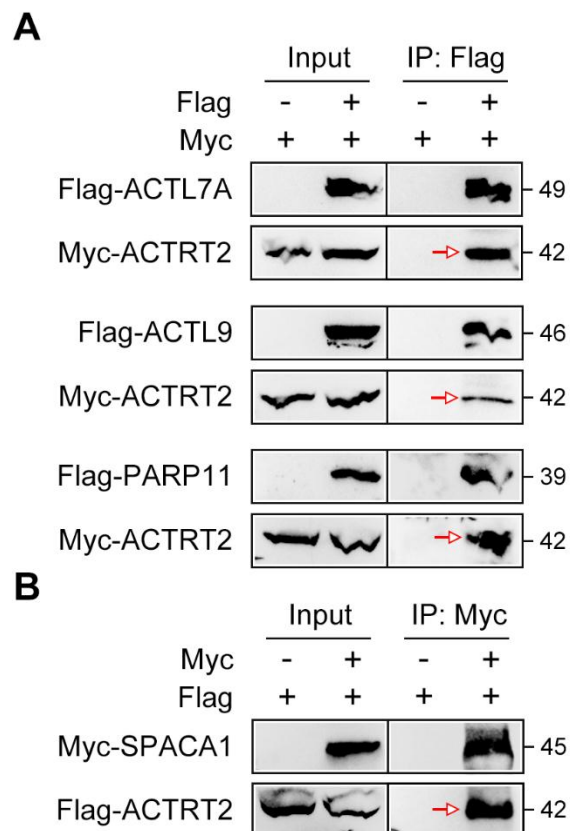
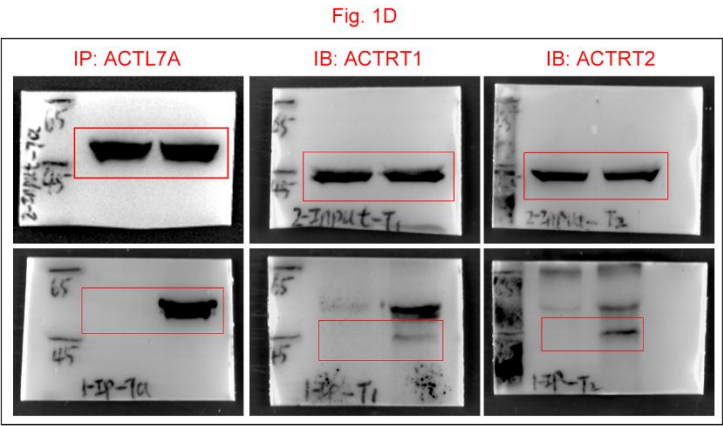
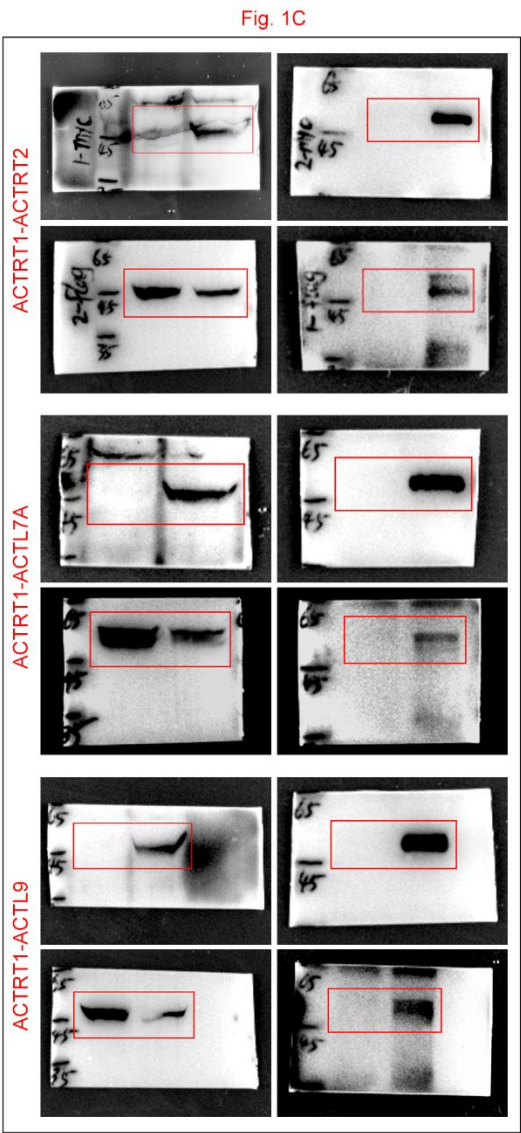
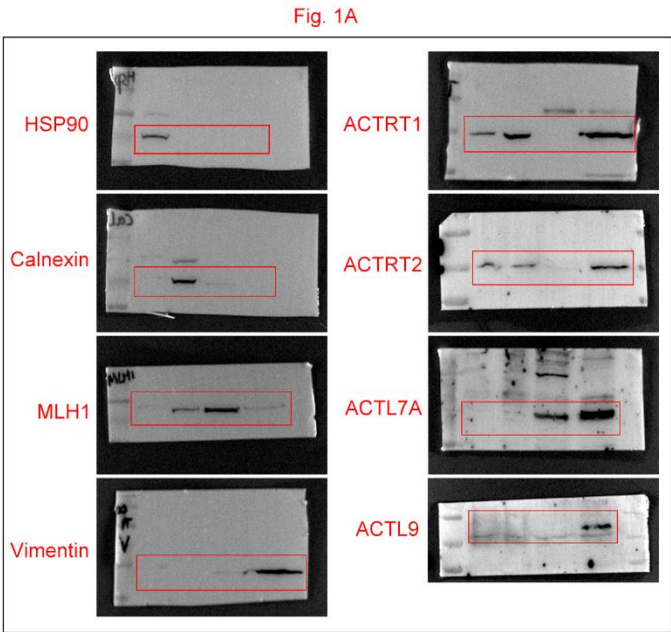


**Fig. S5. ACTRT2 interacts with ACTL7A, ACTL9, PARP11, and SPACA1.** (A) HEK293T cells were transfected with Flag-tagged and/or Myc-tagged recombinant plasmids. Cell lysate was subjected to immunoprecipitated Flag-tagged proteins with anti-Flag antibody. Myc-tagged ACTRT2 could be coimmunoprecipitated with Flag-tagged ACTL7A, ACTL9, and PARP11. (B) Cell lysate was subjected to immunoprecipitated Myc-tagged SPACA1 with anti-Myc antibody. Flag-tagged ACTRT2 could be coimmunoprecipitated with Myc-tagged SPACA1.

Original blots for Fig. 1:



Original blots for Fig. 2A and Fig. 4D:

Fig. 2A

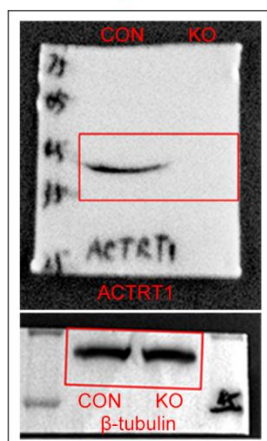
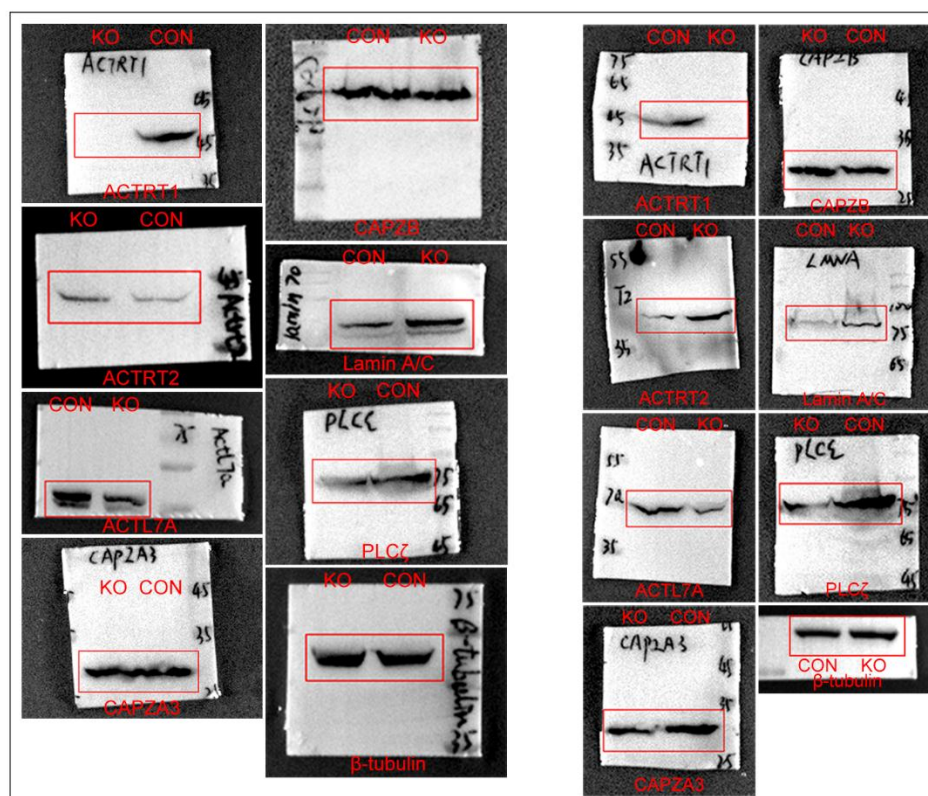


Fig. 4D



Original blots for Fig. 5:

Fig. 5A

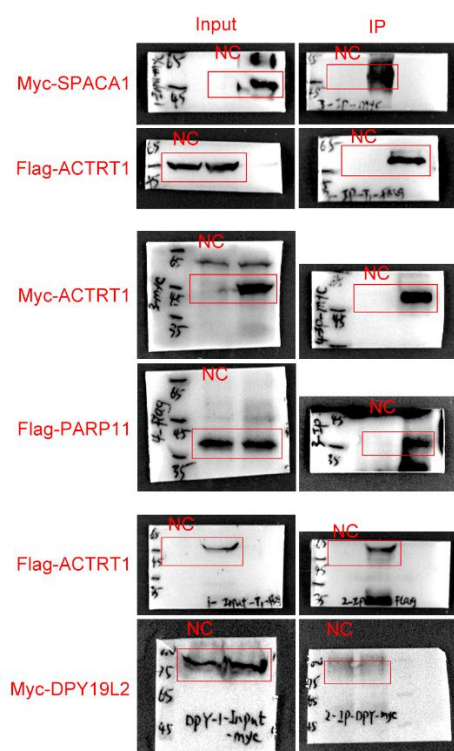


Fig. 5C

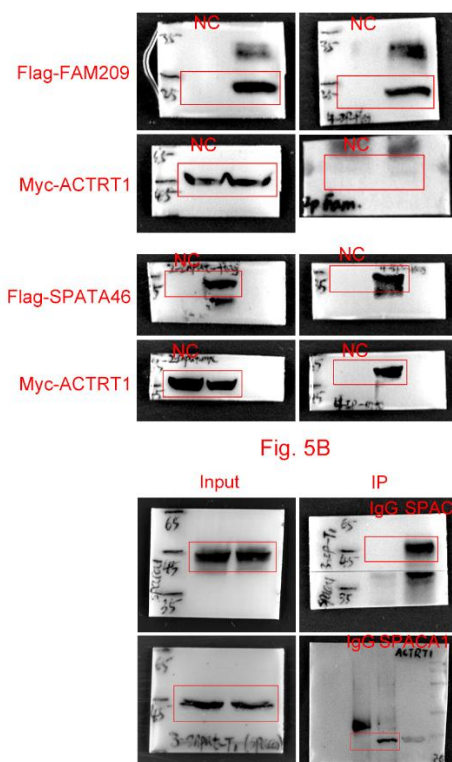
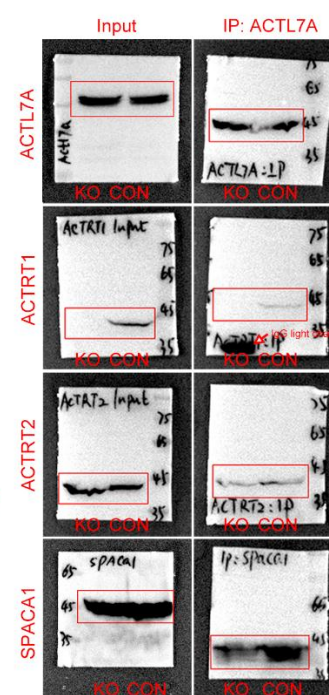
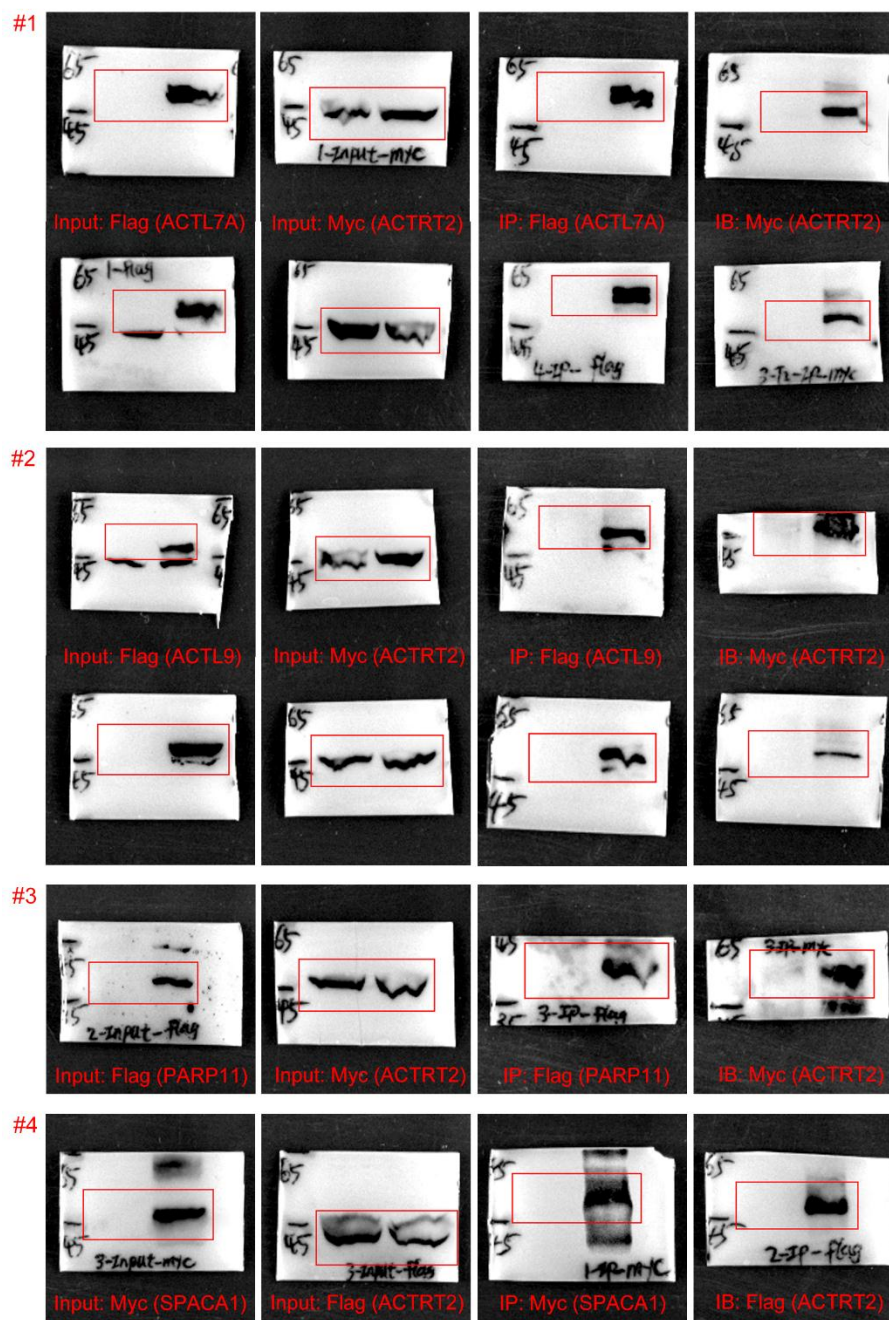


Fig. 5B





Original blots for Fig. S5:



**Table S1.** CRISPR/Cas9 strategy to target mouse *Actrt1* gene. gRNAs are marked in blue, exons are marked in red.

[Click here to download Table S1](#)

**Table S2.** Primers for the genotype of *Actrt1*-KO mice.

PCR No.	Primer No.	Sequence	Band Size
<i>Actrt1</i> <sup>-Y</sup>	F1	TCATCAACACACCCGCAAC	WT: 8230 bp
	R1	CAGTTGGCTACTTGACTTGCCTAG	KO: 297 bp
	F2	GCTAGGAGTGAAACCCAATGAAC	WT: 394 bp
	R2	TTTGTAGCCCAAGGAGACAGTAC	KO: not existed

**Table S3.** Specific primers for amplification of *Actrt1* and *Actrt2* using RT-PCR.

mRNA	Primer No.	Sequence	Band Size
<i>Actrt1</i>	Forward	CATACCATCTGCAAGATCTAATCGG	490 bp
	Reverse	GTTGAGGATGCAGGGGAAGGT	
<i>Actrt2</i>	Forward	CCCCACGGGAGCTAGTCAGAAGAA	512 bp
	Reverse	CATCTTCTGCCCCGCCGAGACA	

**Table S4.** Primers for plasmid construction.

Gene	Primer No.	Sequence
<i>Actr12</i>	Forward	(KpnI) <u>GGTACCCCGACCGGGATGTTTAACCCACTGGT</u>
	Reverse	(XhoI) <u>CTCGAGCGGGAAGCACCGCCTCTGGACCAC</u>
<i>Actl7a</i>	Forward	(KpnI) <u>GGTACCCCGATGTCTCTGGATGGTGTGTGGG</u>
	Reverse	(XhoI) <u>CTCGAGCGGGAAGCACCTTCTGTAGAGGAAGAAAG</u>
<i>Actl9</i>	Forward	(KpnI) <u>GGTACCCCGATGGATGTCAATGGACACCCAAAGT</u>
	Reverse	(XhoI) <u>CTCGAGCGGAAAGTAGCATTTTCGGTATACAACCTGG</u>
<i>Spaca1</i>	Forward	(KpnI) <u>GGTACCATGCGCGCCAGGGGCGC</u>
	Reverse	(XbaI) <u>TCTAGATTTCATTCCATTCACTTAAAGCGTCATCTTCATG</u>
<i>Parp11</i>	Forward	(KpnI) <u>GGTACCATGTTTCACAAGACAGAGGAGTTCTT</u>
	Reverse	(XbaI) <u>TCTAGAGTGGAAGTCTATCAGGTACTCAGGG</u>
<i>Dpy19l2</i>	Forward	(KpnI) <u>GGTACCATGGTGGGGCCGACAAG</u>
	Reverse	(ApaI) <u>GGGCCCCGTTAATCTTCAGTACTCTGTACATACTATTCTG</u>
<i>Fam209</i>	Forward	(KpnI) <u>GGTACCATGCGGACGCTGCTGAGATG</u>
	Reverse	(XbaI) <u>TCTAGACTCAGAGTCCTCCTCCCCCA</u>
<i>Spata46</i>	Forward	(KpnI) <u>GGTACCATGGATAACTACTCACTCCTCAGCAC</u>
	Reverse	(XbaI) <u>TCTAGACTTGAAGGCCTGGCAGCTG</u>

**Table S5.** Antibodies/dyes used in this study.

Protein	Manufacturer	Cat No.	Usage	Concentration
HSP90	Proteintech	13171-1-AP	WB	1:1,000
Calnexin	Abcam	ab133615	WB	1:1,000
MLH1	Proteintech	11697-1-AP	WB	1:1,000
Vimentin	Abcam	ab92547	WB	1:1,000
Myc	Abmart	M20002	WB, IP	1:1,000; 1:100
Flag	Abmart	M20008	WB, IP	1:1,000; 1:100
PNA-FITC	Sigma-Aldrich	L7381	IF	1:500
Mito-Tracker Red	Beyotime	C1049	IF	1:5,000
Actin-Tracker Red	Beyotime	C2203	IF	1:100
Tubulin-Tracker Red	Beyotime	C1050	IF	1:100
ACTRT1	Invitrogen	PA5-31691	WB, IF	1:1,000; 1:200
ACTRT2	Proteintech	16992-1-AP	WB	1:1,000
ACTL7A	Proteintech	17355-1-AP	WB, IP, IF	1:1,000; 1:100; 1:200
SPACA1	Abcam	ab191843	WB, IP	1:1,000; 1:100
CAPZA3	Progen	GP-SH4	WB	1:1,000
CAPZB	Proteintech	25043-1-AP	WB	1:1,000
LMNA	Proteintech	10298-1-AP	WB	1:1,000
PLC $\zeta$	Abcam	ab181816	WB	1:1,000
$\beta$ -tubulin	Abmart	M30109	WB	1:1,000
Alexa Fluor 555-labeled Donkey Anti-Rabbit IgG(H+L)	Beyotime	A0453	IF	1:200
Goat anti-rabbit IgG-HRP	Abmart	M21002	WB	1:10,000
Goat anti-mouse IgG HRP	Abmart	M21001	WB	1:10,000
Rabbit Anti-guinea pig IgG HRP	Abmart	M212124	WB	1:10,000